Journal of Alloys and Compounds 931 (2023) 167530

Contents lists available at ScienceDirect

Journal of Alloys and Compounds

journal homepage: www.elsevier.com/locate/jalcom

Analysis of the thermal stability of residual stresses induced in Ti-6Al-4 V by high density LSP treatments

W. Warzanskyj [a,*], I. Angulo [a], F. Cordovilla [a], M. Díaz [a], J.A. Porro [a], A. García-Beltrán [a], S. Cabeza [b], J.L. Ocaña [a]

[a] UPM Laser Centre. Universidad Politécnica deMadrid. Campus Sur UPM. Edificio La Arboleda. C/ Alan Turing, 1. 28031 Madrid.Spain
[b] Dept. of Diffraction. Institut Max von Laue-PaulLangevin. Avenue des Martyrs 71. 38000 Grenoble. France

ARTICLE INFO

Article history:
Received 23 June 2022
Received in revised form 14 September 2022
Accepted 8 October 2022
Available online 12 October 2022

Keywords:
Laser Shock Processing
Ti-6Al-4 V
Residual Stresses
Mechanical Properties
Surface Properties
Microstructure
Microhardness
Roughness
Dislocation density

ABSTRACT

Laser Shock Processing (LSP) is increasingly applied as an effective technology for the improvement mechanical and surface properties of metallic materials for different types of components, mostly as a means of enhancement of their fatigue life behavior. As reported in previous contributions, a main effect resulting from the application of the LSP technique consists in the generation of relatively deep compression residual stresses fields allowing an improved mechanical behavior. In this paper, the special case of Ti-6Al-4 V alloy is considered with specific consideration of the microstructural changes and residual stresses fields justifying those macroscopic effects. In particular, the effect of the application of different typical LSP intensities on the microstructure and residual stresses fields introduced in this material and their possible correlation to the associated surface effects are analyzed. Emphasis is placed on the study of the thermal stability of these fields after an aging heat treatment at typical high temperature working conditions. The results show that, according to expectations, a certain level of residual stresses and dislocation density remains after in-work thermal aging. The combination of different material characterization techniques has made possible to obtain a correlated set of results highlighting the complementarity of different scale approaches from surface (X-ray) to bulk (neutrons) methods. A model based on the evolution of immobile dislocation density is proposed to rationalize the distribution of dislocation densities, pointing out that plastic deformation is retained. The results clearly show such material improvement stability under typical heavy-duty conditions, thus endorsing the use of the LSP for Ti-6Al-4 V as a suitable technology for industrial applications in relatively high temperature conditions.

1. Introduction

Laser Shock Processing (LSP) is an innovative surface treatment able to induce a layer of compressive residual stress fields under the surface of metallic components. The main recognized effects of the treatment are the enhancement of fatigue, corrosion, and wear resistance of the material [1–6].

LSP is based on the application of high intensity laser pulses on a target following a predefined surface pattern. Typical laser intensity and pulse duration in the “low energy” approach applicable by tabletop commercial lasers are > 1 GW/cm^2 and < 20 ns, respectively [7].

Although initially developed to improve the resistance to fatigue cracking of materials used in aeronautical applications (specifically in aluminum alloys), the LSP technique has shown favorable results in materials such as stainless steels [8] and titanium alloys [9]. This improvement in the lifetime of laser-treated parts has led to numerous industrial applications enabled by the commercial availability of new powerful laser sources capable of delivering pulse intensities above the GW/cm^2 level [2,10]. A significant example of these applications is the LSP treatment of aircraft gas turbine engine components to mitigate foreign object damage (FOD). Other potential applications of LSP are currently being evaluated, namely the treatment of automotive engine components, biomedical implants, and turbine blades in energy power plants.

LSP has been applied to the Ti-6Al-4 V alloy in several studies, which have reported that LSP induces an under the surface strain field and residual compressive stresses that improve friction fatigue and increases microhardness [11] and surface roughness [12].

The Ti-6Al-4 V alloy has low density, high strength, fatigue resistance and formability, and excellent corrosion resistance. This combination of mechanical and physical properties makes it

* Corresponding author.
E-mail address: wsewolod.warzanskyj@upm.es (W. Warzanskyj).

https://doi.org/10.1016/j.jallcom.2022.167530

attractive in different industrial sectors such as the aerospace industry (where it is used for engine components such as compressor blades [13] and where working temperatures are in the range of 400–500ºC [14]). In addition, Ti-6Al-4 V is used in medical prostheses that replace hip, knee, shoulder, and wrist joints, and in dental implants, due to its biocompatibility with the human body [15]. It is normally considered in any application where a combination of high resistance to low to moderate temperatures, light weight and excellent corrosion resistance is required.

In a previous paper by the authors [16], the case of LSP treatment on Ti-6Al-4 V ELI (Extra Low Interstitial) alloy, especially suitable for surgical applications, was reported. The paper presented the results of LSP induced roughness and residual stresses up to a depth of 110 µm, using synchrotron X-ray diffraction.

In this paper, the commercial Ti-6Al-4 V alloy is considered due to its suitability for a wide set of industrial applications. The present study analyzes the microstructural effects induced by the LSP treatment correlating them to the observed residual stresses fields and, specifically, the stability of the observed microstructural properties and residual stress fields under thermal aging cycles, emulating practical service conditions. Different experimental techniques have been combined for the measurement of residual stresses: the good sensitivity at relatively high depths under the treated surface of semi-destructive techniques such as the Hole Drilling Method has been complemented with nondestructive methods (X ray Diffraction and Neutron Diffraction) allowing specific mathematical treatments of the experimental data for the accurate characterization of residual stresses fields in the range form several micrometers under the treated surface to several hundreds of micrometers. This combination of techniques, applied to the treated samples before and after undergoing thermal aging after the LSP treatment, has allowed the understanding of the microstructural phenomena observed in the treated samples, in particular their correlation to hardness and dislocation density, all the obtained results having been found to be fully consistent with the fundamental knowledge acquired by the authors through the analysis of transformed properties of metallic materials subject to LSP processes.

In particular, for the case of alloys such as Ti-6Al-4 V, with potential industrial applications in conditions of relatively high temperatures, the reported results are considered relevant for assuring the working thermal stability of components of such materials under exigent thermal aging working conditions.

2. LSP experimental setup, materials, and characterization methods

2.1. Experimental setup

The irradiation system used for the experiments described in this paper is the same one used in previous contributions by the authors [4, 16–18]. It is shown schematically and photographically in Fig. 1.

The laser source used is a Q-switched Nd:YAG pulsed laser. The laser operates at a frequency of 10 Hz. The FWHM (full width at half maximum) of the generated pulses is 9 ns, the wavelength is 1064 nm (infrared radiation), and the maximum energy is 2.4 J/pulse, which can be reduced with an attenuator. Using a flat mirror and a bi-convex converging lens of a focal distance f = 200 mm, the laser pulse is focused on the target. Both optical components are AR coated for 1064 nm, ensuring high transmittance efficiency. The converging lens is used to control the laser spot diameter on the target, which is set at 1.5 mm. The resulting target power density is > 15 GW/cm^2.

Water is used as a means of confinement and is continuously renewed during the treatment. Water renewal is achieved with a water jet that creates a thin layer of water of constant thickness on the sample to be treated.

The sample is fixed on a support and is driven in the x and y directions by means of an anthropomorphic robot. Predefined pulse overlapping strategies are used for the irradiation of areas of material of approximately 6 cm^2. LSP treatments were performed without coating [1,12,19].

2.2. Materials and treatment strategy

The treated samples were Ti-6Al-4 V rolled plates of 50 × 50×7 mm^3 with the composition shown in Table 1. The samples were treated with LSP (one side) according to the overlapping experimental procedure originally defined by the authors [17,18]. An X-Y equally spaced overlapping scheme was selected which involved an equivalent overlapping density (EOD) of 5000 pulses/cm^2 (overlapping pitch of d = 0.141 mm). Two different pulse sequences were used:

(i) Strategy 1, treating the target treatment area, or patch, with the Peening Direction (PD) parallel to the rolling direction (PD = RD) (L samples).
(ii) Strategy 2, treating the patch with the Peening Direction (PD) perpendicular to the rolling direction, being parallel to the Transverse Direction (PD = TD) (T samples).

The treatments were applied on approximately 25 × 25 mm^2 areas in the central zone of the samples following an alternate scanning strategy. Fig. 2 shows a schematic representation of the treated samples. The samples were treated with LSP and a subset of them thermally relaxed by annealing, giving rise to four types of samples: LB, TB, LC and TC whose characteristics are described in Table 2.

All the samples treated with LSP were previously subjected to a thermal relaxation cycle of 710ºC (beyond the maximum service temperature) for 2 h to avoid any state of stress prior to the LSP treatment. Subsequently, the properties of 2 different types of samples that imply 2 different degrees of thermal/mechanical affectation were analyzed. The LB and TB samples were treated only with LSP with the referred intensity parameters, while the LC and TC samples were subjected to aging/thermal relaxation treatments after the LSP treatment to analyze the effect of working temperatures on the possible relaxation of LSP-induced residual stresses. The LC and TC samples were subjected for 1 h to a heat treatment of 595ºC (close to the working limit of the alloy). The time of 1 h was chosen because in [20] the stress relaxation behavior exhibited by Ti-6Al-4 V over heat treatment temperatures of 500–750 °C was characterized and was found that at 600 °C after 1 h the drop in residual stresses is negligible.

2.3. Characterization methods

The Ti-6Al-4 V alloy samples treated by LSP were characterized for surface roughness, microhardness, microstructure, dislocation density and residual stresses, both before and after the applied thermal aging cycle. The applied annealing was expected to relax the LSP induced modifications, the extent of such relaxation being specifically sought. For that purpose, the analysis of the residual stresses fields has been carried out using different complementary methods (hole-drilling, X-ray diffraction and neutron diffraction) to correctly characterize them from the surface to 1 mm depth.

2.3.1. Surface roughness

The topography of the samples was characterized by means of a Leica DCM3D confocal scanning microscope. Typical parameters as the average surface roughness that corresponds to the arithmetic mean of the absolute values of the ordinates comprised in a sampling surface, S_a, the surface maximum valley depth, $S_{v,}$ and surface maximum peak height, $S_{p,}$ were analyzed [21]. The microscope has a

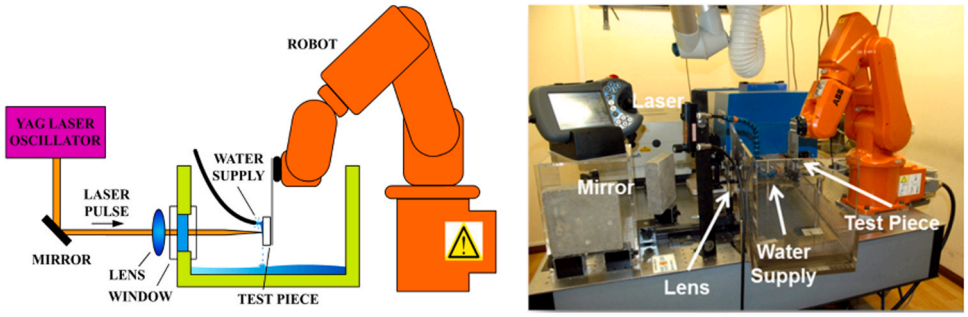

Fig. 1. Schematic representation and photographic view of the LSP irradiation setup used in the reported experiments.

Table 1
Ti-6Al-4 V sample composition analysed by EDS model OXFORD INSTRUMENTS analytical-INCA attached to the SEM microscope used in this study.

Element	Al	V	C	O	Fe	Si	K	Ti
w. (%)	5.83	4.33	0.01	0.12	0.19	0.14	0.01	Bal.

vertical resolution of up to 0.1 µm. The measurements were taken over the entire LSP-treated area. Three measurements were made on each sample.

2.3.2. Microstructure

Concerning microstructure evaluation, a metallographic analysis was performed according to the ASTM E3–11 standard [22] on cross sections of the treated samples. The samples were ground on a Buehler Phoenix® Betagrinding-polishing machine with 400, and 1200 grit/cm^2 size SiC abrasive paper, then polished using 9 µm diamond suspensions to remove surface scratches. Finally, a mirror finish was obtained by polishing with colloidal silica with a diameter of ~0.05 µm. The chemical solution for developing the metallographic samples was a mixture of 90 ml of water, 6 ml of nitric acid, and 4 ml of hydrofluoric acid. The samples were submerged for 30 s in the solution. Microstructures were observed through scanning electron microscopy (SEM) with a FEI INSPECT™ microscope. The voltage and working distance were 20 kV and between 10.1 and 10.8 mm, respectively. Some texture in the RD was found in the samples.

2.3.3. Microhardness

For microhardness characterization, fifteen indentations were made, 70 µm apart from each other, starting 40 µm from the surface of the material to a depth of 1020 µm in the cross-section of the LSP-treated samples. Samples were cut with SiC discs with an automatic linear precision saw model Isomet 4000. A Vickers indenter was used to apply a load of 100 g as prescribed in the ASTM E384 standard [23]. Three indentations were performed at each distance. The hardness tests were carried out with a Matsuzawa hardness tester model MXT30.

Table 2
Samples treatment description.

Sample	Initial treatment (pre LSP)	LSP treatment EOD (cm^{-2})	Thermal aging treatment (post LSP)	Comment
LB	710 °C / 2 h	5000	No	*PD = RD
TB				*PD = TD
LC			595 °C / 1 h	*PD = RD
TC				*PD = TD

*PD ≡ Laser Peening direction; TD ≡ Transverse Direction; RD ≡ Rolling Direction.

2.3.4. Dislocation density

Dislocation density was measured on LSP treated samples with and without post LSP annealing. The measurement was performed following the Williamson and Hall method [24]:

$$\Delta K \cong \frac{0.9}{D} + 0.263 b\sqrt{\rho} \quad (1)$$

where ΔK in nm^{-1} is expressed as $\Delta K = 2\cos\theta(\Delta\theta)/\lambda$. The parameters θ and $\Delta\theta$ stand for the diffraction angle and the difference of the FWHM of the tested sample and a reference one in radians of the XRD peaks, respectively. In this paper, the reference sample is as manufactured with the pre-LSP (PLSP) annealing treatment, but without LSP. And λ is the wavelength of the X-rays (see below the application of XRD technique for residual stress measurements). The

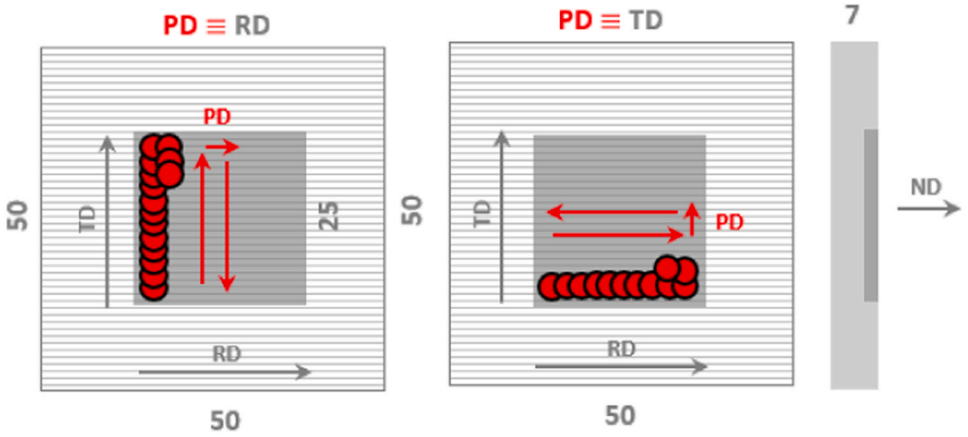

Fig. 2. Detailed scheme of treated samples. Red circles are the overlapping laser spots. Left: peening direction coincident with the manufacturing rolling direction. Right: peening direction transversal to the manufacturing rolling direction. Dimensions are in mm.

parameters 0.9, D, b and ρ represent the Scherrer constant, crystallite size, Burgers vectors and dislocation density in a material. Crystallite size can be qualitatively measured based on the Scherrer equation [25]:

$$D = \frac{0.9\lambda}{\Delta\theta\cos\theta} \tag{2}$$

Combining Eqs. (1) and (2), the following expression is obtained for the dislocation density:

$$\rho = \left(\frac{\cos\theta(\Delta\theta)}{0.263b\lambda}\right)^2 \tag{3}$$

2.3.5. Residual stresses

Residual stress fields induced by the LSP treatment (the crucial objective in the analysis) were measured by three complementary techniques: the hole-drilling method, X-ray diffraction and neutron diffraction. Through the combined use of the three methods the assessment of residual stress fields in the close-to-surface (XRD), intermediate (HD) and deep (ND) penetration ranges up to depths exceeding 1 mm were aimed to be determined in a consistent way. As the only possible limitation to this consistency, each technique was applied to a different group of samples, a potential source of divergence that, however, has been observed to be lower than the level of measurement uncertainty associated individually to each of the three methods employed.

The first method used for the measurement of residual stresses was the hole-drilling (HD) strain gage method according to the ASTM standard E837 [15]. It is a widely used technique for the determination of in-depth residual stress profiles induced by LSP [26]. Measurements were performed at the treated surface points and surrounding areas obtaining in depth profiles to a maximum depth of 1.0 mm. To define the residual stress profiles, the measurements at the following seven depths are taken: 0.013, 0.060, 0.120, 0.230, 0.400, 0.620 and 0.913 mm. These are the chosen depths because they are the ones that optimize the residual stress profile calculation algorithm, as shown in [27]. Three different rounds were performed, and their values averaged at every depth, to assure measurement reliability. The final residual stress distribution in depth was determined using H-drill v. 2.33 software (integral method) [28]. This technique can measure the in-plane residual stresses in all the in-plane directions. For making comparisons between the measurements obtained by the different techniques, the maximum and minimum in-plane Mohr stresses were considered.

The surface residual stresses were complementarily measured nondestructively by XRD applying the $\sin^2\psi$ method [29,30] at the facilities provided by the IMDEA Materials institute with an Empyrean, PANalytical X-ray diffractometer. The crystallographic plane family {213} of the hexagonal close packing (HCP) α phase and Bragg's angle ($2\theta \approx 142^o$) obtained by Cu K_α radiation ($\lambda = 1.541838$ Å) were employed for this purpose. Residual stresses were measured on the sample surface in directions corresponding to $\varphi = 0$, 60 and 120º, being $\varphi = 0^o$ the RD. To perform measurements for different depths, the measured surface was progressively eroded by electro-polishing with nominal depth steps of 50 µm. Electro-polishing was performed in a solution of A3 electrolyte consisting of 70% methanol, 10% 2-butoxyethanol, 3% perchloric acid and 17% water. Material removal at each electro-polishing round was determined by the voltage applied between the solution and the sample bottom surface, namely 38 V, and the average duration, 1.5 min. This timing was obtained by trial and error in dummy samples.

The diffraction elastic constants (DECs) used for calculating the stresses from the strain measurements were calculated according to Kröner model [31]. A simple and accurate approach to the Kroner model can be adopted by averaging the Reuss and Voigt estimates. Voigt assumed each grain to experience the same strain field (continuity of strain at the grain boundaries) resulting in a variation of stress from grain to grain. With this approach the X-ray elastic constants $S_1 = -\nu/E$ and $1/2S_2 = (1+\nu)/E$ for hexagonal crystals are obtained according to [32]:

$$S_{1V} = \frac{-3(C_{11} + C_{33} - 4C_{44} + 5C_{12} + 8C_{13})}{(7C_{11} + 2C_{33} + 12C_{44} - 5C_{12} - 4C_{13})(2C_{11} + C_{33} + 2C_{12} + 4C_{13})} \tag{4}$$

$$\frac{1}{2}S_{2V} = \frac{15}{7C_{11} + 2C_{33} + 12C_{44} - 5C_{12} - 4C_{13}} \tag{5}$$

In contrast, Reuss assumed each grain experienced the same stress field (continuity of stress at the grain boundaries) resulting in a variation of strain from crystallite to crystallite. For hexagonal crystals, the corresponding values are obtained according to [32]:

$$S_{1R} = \frac{1}{2}[S_{12} + S_{13} + (2S_{13} - S_{11} - S_{33} + S_{44}) H^4 - (S_{13} - S_{11} - S_{33} + S_{44} + S_{12})H^2] \tag{6}$$

$$\frac{1}{2}S_{2V} = \frac{1}{2}[2S_{11} - S_{12} - S_{13} - 3(2S_{13} - S_{11} - S_{33} + S_{44}) H^4 + (5S_{13} - 5S_{11} - S_{33} + 3S_{44} + S_{12})H^2] \tag{7}$$

$$H^2 = \frac{l^2}{\frac{4}{3}\frac{c^2}{a^2}(h^2 + hk + k^2) + l^2} \tag{8}$$

Here (hkl) are the Miller indices of the investigated lattice plane, {213} of the HCP α phase, and c and a are the constants of the hexagonal lattice of titanium. The quotient c/a is the corresponding to the hexagonal compact system, $2(2/3)^{1/2}$. C_{ij} are the elastic stiffness constants while S_{ij} are the elastic compliance constants. For the treated material, the elastic constants used are found in [33].

The calculated DECs were $1/2\ s_2 = 11.28\ 10^{-6}$ MPa^{-1} and $s_1 = -2.75\ 10^{-6}$ MPa^{-1}, that correspond to a Youngs modulus value of 117.3 GPa and Poisson coefficient value of 0.323, similar than the ones reported in the literature [30]. In alloys with more than one phase, residual stresses are balanced between the different phases. This also happens in this alloy, but, as is shown in the next section, in the considered samples β phase volume fraction is less than 10% and its contribution (considering its DECs) is not critical, so it can be considered that residual stresses in the α phase are representative of the ones in the entire alloy.

For the reported XRD determinations, 7 different tilt angles between $0° < \psi < 51°$ [29], with step sizes being equidistant to $\sin^2\psi$, were applied. Stress relaxation and redistribution due to material removal were calculated by the Moore and Evans procedure [33]. To calculate strains by the X-ray diffraction method, a reference d_0 must be selected. In this case, an annealed sample without LSP was also measured at the surface to compare the impact of LSP. For making comparisons between measurements obtained by the different techniques, the maximum and minimum in-plane stresses and stresses in the RD and TD were considered.

Finally, neutron diffraction measurements were performed at SALSA strain diffractometer [34] at the public European facility Institute Laue-Langevin (ILL), in Grenoble, France. Fig. 3 shows a scheme of the experimental setup. The neutron wavelength used was $\lambda = 1704$ Å and the gauge volume (GV) defined by radial collimators was $0.6 \times 0.6 \times 10$ mm^3. Entry scans were performed in order to disclose strain values close to the surface by applying a pseudo-strain correction for partially immersed GV, continuing in line scans into the bulk of the plate. To obtain the neutron diffraction measurement positions, two situations are considered. The first one,

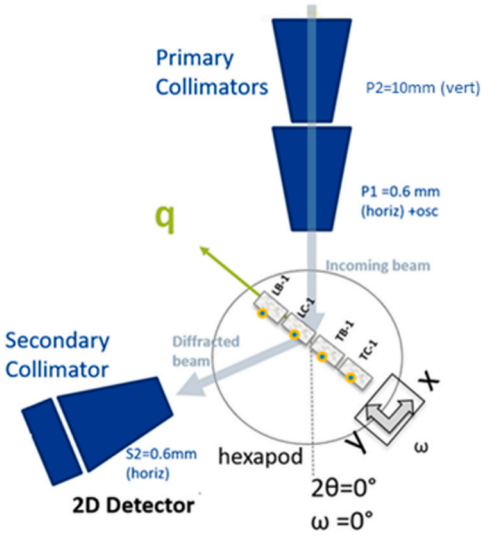

Fig. 3. Top view sketch of the experimental setup of the neutron diffraction experiment detailing the incoming and diffracted vectors with the resulting **q** (i.e., strain component).

when the GV is partially immersed. In this case, the position is obtained with SALSAs hexapod position with a precision of ± 5 µm [34] and the pseudo-strain correction is applied to correct the centroid position and beam intensity [35–37]. In the second case, when the GV is totally immersed, the position is obtained with the hexapod position with a precision of ± 5 µm. To calculate strains by the neutron diffraction method, the reference d_0 was selected as the corresponding to the bulk untreated material condition in the middle of the plate on the far field from LSP. Then, to obtain the final values of residual stresses, Hooke's Law is used for each specific hkl strain experimental values and similar DECs as obtained for X-ray method. A complete 2θ scan was performed to obtain the crystallographic planes that would provide the best compromise between diffraction peak acquisition time and peak quality. It was observed that some crystallographic planes gave significant differences in the intensity (even extinctions), confirming the texture of the samples. The lattice planes selected were α pyramidal {101} at 2θ = 45° for the RD and {002} α basal at 2θ = 42° for the TD. The normal component could not be obtained due to signal extinctions emphasizing the strong texture condition. Hence, the hypothesis is assumed that the principal stresses are very similar to the ones in the RD and TD, whereas the ND is assumed to be neglectable, i.e.: $\sigma_{i3} = 0$; (i = 1, 2, 3. RD ≡ 1, TD ≡ 2, ND ≡ 3).

The applicable expression of the Hooke's law is (9):

$$\sigma_i = \left[\frac{E_{hkl}(1-\nu_{hkl})}{(1+\nu_{hkl})(1-2\nu_{hkl})}\right]_i \varepsilon_i + \left[\frac{E_{hkl}\nu_{hkl}}{(1+\nu_{hkl})(1-2\nu_{hkl})}\right]_j \varepsilon_j + \left[\frac{E_{hkl}\nu_{hkl}}{(1+\nu_{hkl})(1-2\nu_{hkl})}\right]_k \varepsilon_k \quad (9)$$

where i, j, k ≡ RD, TD, ND; i ‡ j ‡ k. As in the X-ray diffraction method, the Reuss and the Voigt hypotheses were considered as the limits between which the residual stresses are found. For Reuss and Voigt hypothesis, E_{hkl} and ν_{hkl} can be calculated from Eqs. (4)–(8). In the Voigt hypothesis, $E_{hkl} = E$ and $\nu_{hkl} = \nu$, for all h, k, l. In the Reuss hypothesis, different E_{hkl} and ν_{hkl} must be calculated for the different measured directions as measurements were made in different diffraction planes.

For the ND, two diffraction planes were considered: the ones for which E_{hkl} and ν_{hkl} have maximum and minimum values, respectively, to ensure that the resulting residual stresses are within the limits determined by these assumptions. These planes are {100} for minimum E_{hkl} and maximum ν_{hkl}, respectively, and {002} for maximum E_{hkl} and minimum ν_{hkl}, respectively [38]. Even considering $\sigma_{ND} = 0$, we need the component ε_{ND} to be able to calculate the stresses in the RD and TD. ε_{ND} is obtained assuming $\sigma_{ND} = 0$, but we also need the DECs in the ND to be able to calculate it. Hence these assumptions must be made for the DECs in the ND. The nominal value of the residual stresses is calculated as the average of the Voigt value and the average of the two Reuss values. Considering that the strains have been obtained by means of a non-conventional method (different crystallographic planes for RD and TD), the calculated residual stresses provide a tentative estimation. Applying the pseudo-strain correction mentioned above, strain values have been obtained at depths of up to 31 and 27 micrometres from the surface for the LB and TB samples, respectively. However, in LC and TC samples it was possible to obtain good quality measurements right at the surface.

3. Experimental results and discussion

In this section, the results of the measurement performed on LSP treated samples before and after annealing are presented.

3.1. Surface roughness

The 3D surface topology of flat unpeened samples and LSP treated samples is presented in Fig. 4. The values of surface roughness (S_a), deepest valley (S_v) and highest peak (S_p) of the samples are listed in Table 3. First, the three parameters considerably increase when As Manufactured samples are thermally treated before the LSP treatment. As reported in a previous paper [16], such a treatment yields the formation of a continuous and dense layer containing submicrometric rutile-type oxides, which, accordingly with the oxidation behavior of the treated material, will be very thin (< 1 µm). This thickness agrees with the roughness difference between both states.

Regarding the surface treated with LSP, laser treatment induces the formation of a continuous Ti-oxide layer that looks like a pancake of melted drops rounded by isolated cavities of small size, associated to places where sublimation took place. Occasionally, such cavities are linked by small cracks. Such oxidation is consistent with the short but severe thermal effect associated to the laser processing. TiO is formed [39], which is a metastable oxide structure likely developed as consequence of the local high temperature achieved during laser processing and further fast cooling due to the low temperature of the thicker metal substrate [16]. These features explain the considerable increase of the roughness parameters.

Further annealing of the laser treated samples in a furnace operating at 500–700 °C in air [39] allows the approach of this oxide to the stable forms, likely to rutile. In the post-LSP annealing treatment at 595ºC such transformation takes place and resembles the nanocrystals developed prior to the laser treatment [16]. This fact may explain the slight increase in the deepest valley and highest peak values. Roughness minimally decreases with respect to the non-thermal treated samples post-LSP but, considering the roughness measurement uncertainty, this reduction may be neglected. The roughness variation produced by the LSP treatment is practically unaffected by the subsequent heat treatment.

3.2. Microstructural characterization

The micrographs of samples treated with LSP taken by scanning electron microscopy are presented in Fig. 5. Only the first few hundred microns below the treated surface are shown. The interior of the material has a microstructure identical to that of the material in its basic state. Nor is any phase change expected, because the LSP treatment is a fundamentally mechanical process located in the first

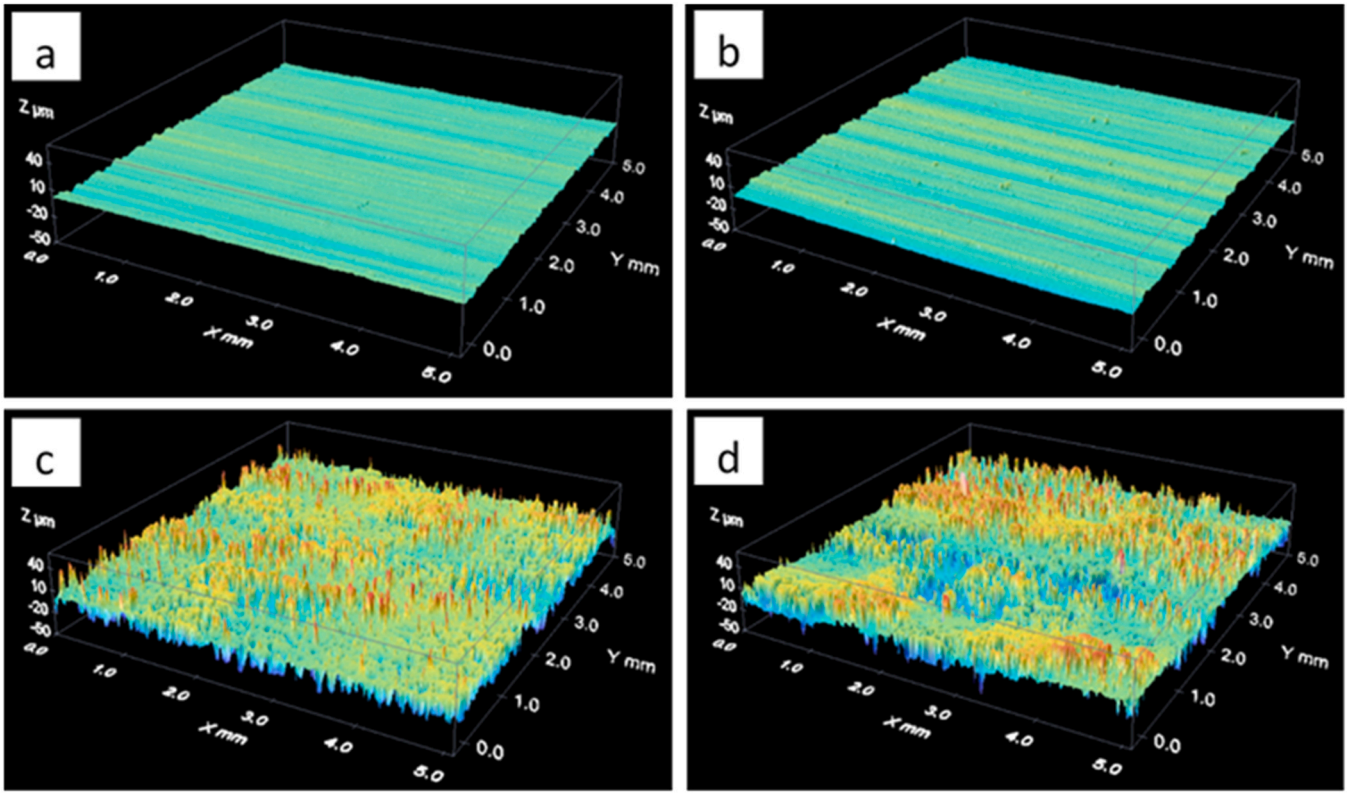

Fig. 4. Topographic Confocal Microscope images showing the changes in surface roughness induced by the LSP technique for Ti-6Al-4 V: (a) As manufactured, (b) Pre LSP thermal treated, (c) LSP treated (LB/TB), (d) LSP and post LSP thermal treated (LC/TC).

Table 3
Surface roughness parameters measured for Ti-6Al-4 V with the different treatments.

Roughness			
	S_a (µm)	S_v (µm)	S_p (µm)
As Manufactured	1.740 ± 0.029	9.601 ± 1.054	9.856 ± 0.873
Pre LSP thermal treated	2.097 ± 0.124	15.142 ± 3.507	15.421 ± 3.313
LSP treated (LB/TB)	8.987 ± 0.307	47.814 ± 1.406	63.735 ± 11.812
LSP + post LSP thermal treated (LC/TC)	8.669 ± 0.176	51.868 ± 4.165	77.744 ± 17.813

layers of the material [40]. There appear also some thermal effects, but right on the surface, to a depth of < 1 µm, where an oxide film [16] is formed. The microstructure shows almost equiaxed hexagonal-close-packed (HCP) primary α grains and ~10% volume fraction of body-centered-cubic (BCC) intergranular β phase [41,42]. The α phase grains appear elongated showing that the samples were rolled and, therefore, present texture in the RD.

No slips, twinning or internal cracks are observed in any of the LSP samples, but a grain size reduction is observed due to the LSP treatment. Fig. 6 shows the average grain size, obtained by the intersection method [43], with respect to depth, of the samples in the pre-LSP condition (PLSP), LSP condition and LSP + heat treated condition. There is a clear reduction in the grain size due to the LSP process in the first ~20–40 µm below the surface, reaching even a reduction of 80% in the immediate vicinity of the surface. In the same way, the post LSP heat treatment increases the grain size reduced by the LSP treatment. A 20% grain size increase, approximately, is observed due to the post LSP annealing in the area where the grain size reduction due to LSP occurs. These results are coherent with reported in [44–46]. In a previous paper of the authors [44] it was observed a relative material compaction due to LSP treatment in the SEM transverse cuts of Ti-6Al-4 V. Guo et al. [45] reported an average grain size decreasing from 33.6 to 24.3 µm due to grain refinement effect caused by LSP in laser additive manufactured Ti-6Al-4 V samples. Ranjith Kumar et al. [46] showed a clear variation in grain size at the surface and below the surface of all laser peened Ti-6Al-4 V samples.

The fact that no twinning is observed in any of the LSP samples contrasts with other treatments, where twinning appears. To explain the absence of twinning in the LSP samples, the idea proposed in [47] is accepted, that twinning appears in high strain rate processes but only till a strain rate threshold, whose value has not been studied in depth, but that seems to be approximately 10^4 s^{-1}. And in LSP processes, strain rates are in the range of 10^4-10^6 s^{-1} are generated in the material [4–6]. This is coherent with the grain size reduction observed due to LSP and is also explained in [47]. LSP increases in this material the dislocation density and networks of dislocation cells and sub grains are formed.

3.3. Microhardness

As Manufactured Ti-6Al-4 V presents noticeable microhardness, that severely degrades with industrial use or high temperatures, annealing. So, for practical applications, the microhardness after use/annealing specs should be considered, to forestall unexpected failures due to microhardness degradation.

The depth hardness profile for Ti-6Al-4 V for the considered treatment states is shown in Fig. 7. The microhardness of the Ti-6Al-4 V As Manufactured right on the surface is ~356 HV. This microhardness drops to ~350 HV along the first millimetre of depth. After the PLSP thermal treatment, the microhardness is reduced to ~291.5 HV on the surface and to 280 HV one millimetre deep, a reduction of 18–20%. At the surface of the treated sample, the LSP process increases microhardness up to ~370 HV, what represents an increase

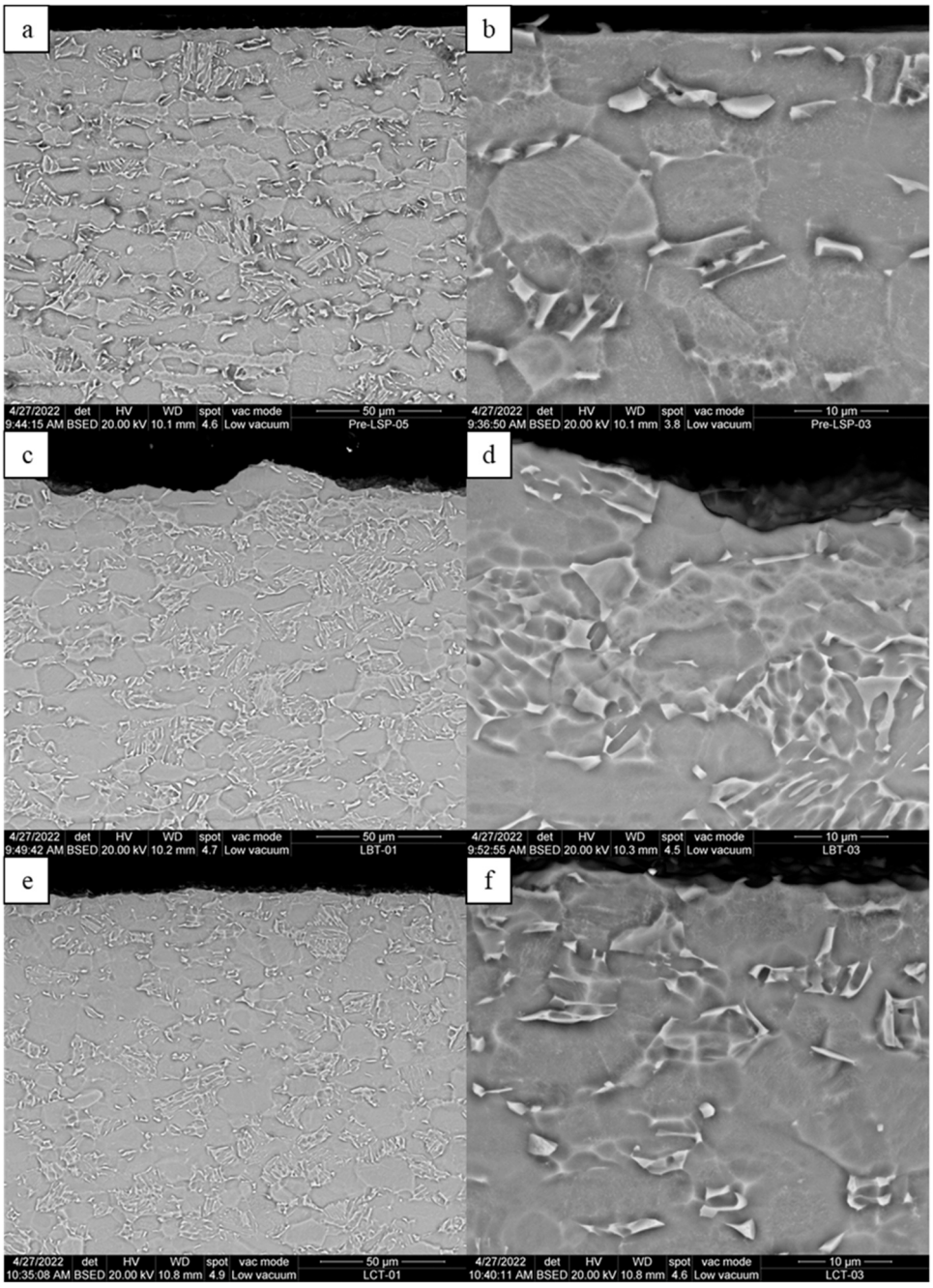

Fig. 5. Microstructure of the cross-section of Ti-6Al-4 V samples treated with LSP in the PLSP, LSP-treated and LSP + heat treated conditions observed by BSED SEM microscopy: (a)-(b) PLSP, (c)-(d) LSP-treated and (e)-(f) LSP + heat treated.

of 27% with respect to the thermal treated sample and of 4% with respect to the alloy As Manufactured. After the Post-LSP heat treatment, the microhardness is reduced to ~315 HV at the surface, which means a reduction of 15% with respect to the LSP-treated samples without subsequent heat treatment. At a depth of one millimeter, the microhardness of the material in this treated state is ~287 HV. However, the microhardness of the annealed samples after the LSP treatment retain an increase of around an 8% with respect to the material in the PLSP state in the surface and remains slightly higher at a depth of one millimeter. Microhardness decreases gradually in depth-wise since the intensity of compressive stress waves decreases along the depth from the peened surface.

Results of other authors also indicate that the microhardness of Ti-6Al-4 V samples is improved via LSP. Nalla et al. [40] found that the LSP can provide a greater than 10% increase in hardness near the surface. Peyre et al. [3] showed that LSP is a suitable process to acquire higher microhardness and a large depth of the affected layer. Other reports [48–51] have shown that LSP induces varying levels of plastic deformation, for which microhardness is an indirect marker.

3.4. Dislocation densities

On untreated samples, dislocation density is negligible, on the order of 10^8 cm^{-2} [52]. The observed increase in microhardness due to the LSP treatments is attributed to the increase of dislocation density induced by this treatment. Dislocation reinforcement theory demonstrates the contribution of dislocation density for improving

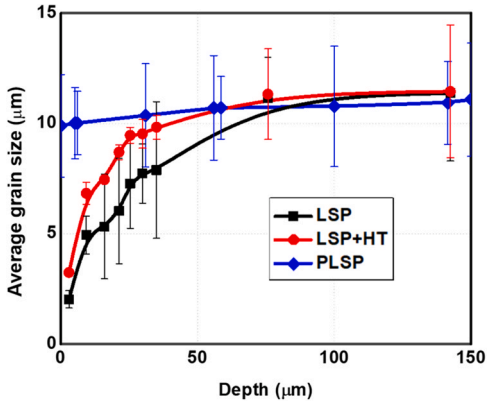

Fig. 6. Average grain size, obtained by the intersection method, with respect to depth of Ti-6Al-4 V in the PLSP, LSP-treated (LB/TB) and LSP + heat treated (LC/TC) conditions.

the hardness of the material [53]. High-density dislocations tangle together and prevent the generation and movement of other dislocations during plastic deformation; thus, microhardness is improved [54].

In hexagonal crystal systems such as the ones for Ti-6Al-4 V there are three different major slip systems that are related to the three glide planes: basal (Type < a > dislocations), prismatic (Type < c > dislocations) and mixed or pyramidal (Type < c+a > dislocations) [24]. More than one sub slip system is activated during plastic deformation of this material. Dislocations may also be populated in more than one slip system. Several proportions have been proposed. In the work of Simm [54], < a > dislocations are most frequent (~84%) while < c > dislocations were absent. Dragomir and Ungar proposal [24] of dislocation population fractions is of 75%, 20% and 5% for < a > , < c > and < c+a > dislocations, respectively.

There are three fundamental Burgers vectors in the material associated to the three types of dislocations (< a > , < c > , < c+a >). The magnitude of these vectors in case of hcp titanium are 0.295 nm, 0.468 nm and 0.553 nm for, Type < a > dislocations, Type < c > dislocations and Type < c+a > dislocations, respectively [55]. The magnitude of b used in Eq. (3) must be an average of the three values mentioned. Based on the hypothesis of Simm [56], as seen before, b = 0.33628 nm. This value is close to the one obtained in Dragomir and Ungar [24] of 0.3425 nm for his hypothesized dislocation population fractions.

Following the Williamson and Hall method, Fig. 8 shows the dislocation density profile with depth for four different samples, LB and TB without annealing and LC and TC with annealing. High density values on the material surface are beneficial since they translate into improved mechanical properties. After annealing dislocation density on the surface is approximately $4{\cdot}10^{11}$ cm^{-2}, well above that of untreated samples.

There are two sorts of dislocations, mobile and immobile dislocations. The mobile dislocation density is assumed to be much smaller than the immobile density according to [57]. The model for evolution of the immobile dislocation density has two parts: hardening and restoration. In the following equations, z refers to depth from the surface.

$$\dot{\rho}_i(z) = \dot{\rho}_i^{(+)}(z) - \dot{\rho}_i^{(-)}(z) \tag{10}$$

It is assumed that mobile dislocations move, on average, a distance Λ (mean free path) before they are immobilized or annihilated. According to the Orowan equation [58], density of mobile dislocations and their average velocity are proportional to the plastic strain rate. It is reasonable to assume that increase in immobile dislocation density also follows the same relation [59]. This leads to:

$$\dot{\rho}_i^{(+)}(z) = \frac{m}{b}\frac{1}{\Lambda(z)}\dot{\bar{\varepsilon}}^p(z) \tag{11}$$

where m is the Taylor orientation factor and b is the Burger's vector of the dislocation. The mean free path can be computed from the grain size (g) and dislocation sub cell or sub grain diameter (s) as:

$$\frac{1}{\Lambda(z)} = \frac{1}{s(z)} + \frac{1}{g} + \text{others} \tag{12}$$

where others denote contributions from obstacles like precipitates, interstitial elements, martensite lathes, etc. Models for recrystallization, grain growth, precipitation, dissolution, etc., can be included here [60]. In this model, only grains and sub grains are considered. The formation and evolution of sub cells has been modeled using a relation proposed by Holt [61].

$$s(z) = \frac{K_c}{\sqrt{\rho_i(z)}} \tag{13}$$

Annihilation and remobilization of dislocations are thermally activated reorganization processes that lead to restoration of the deformed lattice [62]. In high-stacking fault materials, recovery process might balance the effects of strain hardening leading to a constant flow stress. The density of immobile dislocations is reduced during recovery process due to glide, climb [63] and globularization, but this last phenomenon only takes place at elevated temperatures (650–815 °C) [64] that are not considered in this paper. The term which is controlled by glide is proportional to the current dislocation density and the plastic strain rate, and is formulated as [57,65]:

$$\dot{\rho}_{i\,(glide)}^{(-)}(z) = \Omega\rho_i(z)\dot{\bar{\varepsilon}}^p(z) \tag{14}$$

where Ω is a dimensionless optimization recovery function that depends on temperature. This equation takes only dynamic recovery

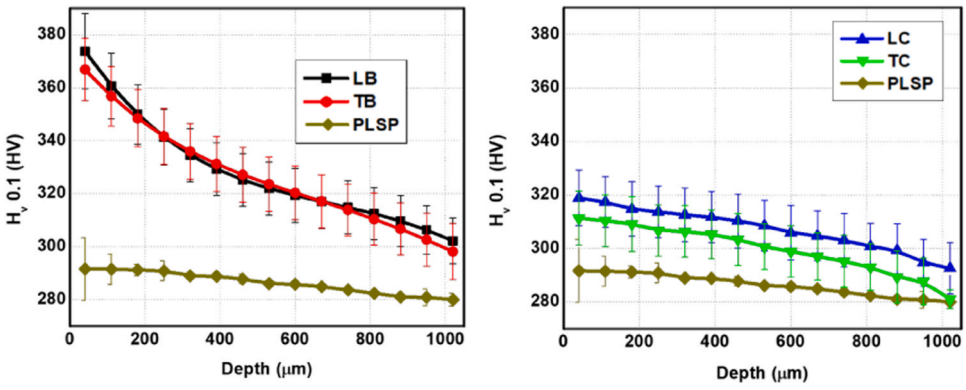

Fig. 7. Hardness variation of Ti-6Al-4 V with the depth for the material. Left: PLSP and LSP treated (LB/TB). Right: PLSP and LSP + post LSP thermal treated (LC/TC).

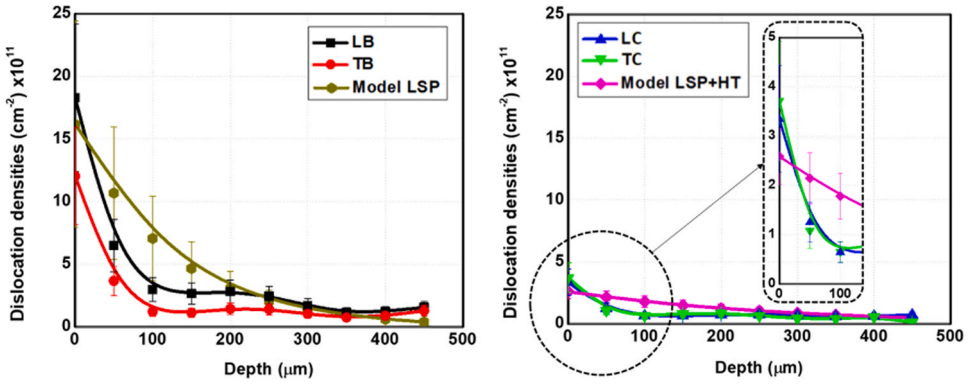

Fig. 8. Dislocation density in Ti-6Al-4 V as a function of depth for the treatments studied. Left: dislocation densities of samples LSP treated and the dislocation density hardening model. Right: dislocation densities of samples LSP treated and post-LSP heat treated and the remaining dislocation density model.

into the consideration due to the strain rate. Static recovery, however, is controlled by diffusion climb having the following formulation [66,67]:

$$\dot{\rho}_i^{(-)}{}_{(climb)}(z) = 2c_\gamma D_{app}(z)\frac{Gb^3}{kT}(\rho_i(z)^2 - \rho_{eq}{}^2) \tag{15}$$

where c_γ is a calibration parameter, D_{app} is the apparent diffusivity, G is the temperature dependent shear modulus, k is Boltzmann's constant, T is the temperature and ρ_{eq} is an equilibrium limiting value of dislocation density. Mathematical and modeling details about D_{app} term can be found in references [66–70]. According to the model proposed by Porter and Easterling [70], Militzer et al. [67], the apparent diffusivity can be written as:

$$D_{app}(z) = D_l(z) + N(z)D_p \tag{16}$$

Diffusion occurs by the motion of defects like vacancies and interstitial atoms and by atomic exchange. But vacancy motion is the predominant diffusion mechanism, due to the lower activation energy of vacancy migration [71]. The self-diffusivity D_l is the product of vacancy diffusivity and its equilibrium concentration. This can be rewritten generically for any concentration of vacancy as:

$$D_l(z) = \frac{c_v(z)}{c_v{}^{eq}}D_v \tag{17}$$

Where $c_v{}^{eq}$ and c_v are the equilibrium and current vacancy concentration, D_v is the self-diffusion coefficient. Lattice diffusivity of α and β phases differ by many orders of magnitude, which results in a jump at the β-transus temperature [72]. This transition is modeled by scaling the diffusivity with the volume fraction of each phase.

$$D_l(z) = \frac{c_v(z)}{c_v{}^{eq}}[D_\alpha(1-f) + D_\beta f] \tag{18}$$

where f = f(T) is the volume fraction of β phase. The effect of phase change on vacancy concentration is ignored here. Knowing the β-transus temperature and that at room temperature f ≈ 0.1, f(T) can be expressed as:

$$f(T) = 1 - \frac{T_{\beta-transus} - T}{T_{\beta-transus} - T_{room}}0.9 \tag{19}$$

Lattice diffusion is responsible for climb at high temperatures. However, at intermediate temperatures, diffusion along dislocation lines, referred to as core or pipe diffusion, has a larger effect on climb [73]. While studying the static grain growth of fine-grained Ti-6Al-4 V, Johnson et al. [74] concluded that grain boundary and pipe diffusion are the controlling mechanisms at temperatures less than 0.5 T_{melt} (800 °C). The effect of grain boundary diffusion can be neglected in the proposed model because of the larger grain size of the material considered. Reed-Hill [75] proposed an Arrhenius-type equation for grain boundary diffusion. Since the basic mechanisms of grain boundary and dislocation core diffusion are the same [76], a similar formulation can be employed here.

$$D_p = D_{p0}e^{-\frac{Q_p}{kT}} \tag{20}$$

where, D_{p0} is the frequency factor and Q_p is the activation energy. The total diffusive flux in the material is enhanced by the short circuit diffusion, which is dependent on the relative cross-sectional area of pipe and matrix, parameter N in Eq. (12).

$$N(z) = \frac{n_a{}^p}{N_a{}^l}\rho_i(z) \tag{21}$$

where, $n_a{}^p$ is the number of atoms that can fill the cross-sectional area of a dislocation and $N_a{}^l$ is the number of atoms per unit area of lattice. When subjected to deformation or temperature change, materials generate excess vacancies. Creation of vacancy increases entropy, but consumes energy, and its concentration increases with temperature and deformation. The concentration of vacancies attain equilibrium if left undisturbed in isothermal conditions. The model considered here is only concerned with mono-vacancies. The equilibrium concentration of vacancies at a given temperature, according to [75,77] is

$$c_v{}^{eq} = e^{\frac{\Delta S_{vf}}{k}}e^{-\frac{Q_{vf}}{kT}} \tag{22}$$

where, ΔS_{vf} is the increase in entropy while creating a vacancy and Q_{vf} is the activation energy for vacancy formation. In reference [67] a model for excess vacancy concentration with generation and annihilation components was proposed. That model can be written as:

$$\dot{c}_v(z) - \dot{c}_v{}^{eq} = \left(\chi\frac{m\alpha Gb^2}{Q_{vf}}\sqrt{\rho_i(z)} + \zeta\frac{c_j}{4b^2}\right)\frac{\Omega_0}{b}\dot{\varepsilon}^p(z) - D_{vm}\left(\frac{1}{s(z)^2} + \frac{1}{g^2}\right)(c_v(z) - c_v{}^{eq}) + c_v{}^{eq}\left(\frac{Q_{vf}}{kT^2}\right)\dot{T} \tag{23}$$

Here, α is a proportionality parameter, χ is the fraction of mechanical energy spent on vacancy generation, Q_{vf} is the activation energy of vacancy formation, ζ is the neutralization effect by vacancy emitting and absorbing jogs, c_j is the concentration of jogs, Ω_0 is the atomic volume, D_{vm} is the diffusivity of vacancies, g is the grain size, s is the sub cell diameter and $\dot{T}$ is the time derivative of the temperature field. As only dislocation density evolution at a constant temperature is studied, $\dot{c}_v{}^{eq} = \dot{T} = 0$.

$$\zeta = 0.5 - 10c_j, \quad c_j = e^{-\frac{Q_{jf}}{kT}}, \quad Q_{jf} = \frac{Gb^3}{4\pi(1-\nu)} \tag{24}$$

where Q_{jf} is the activation energy of jog formation. During the LSP process, hardening equilibrates with recovery by glide and

Table 4
Parameters of the dislocation density model.

Parameter	Units	Value	Reference
m	–	2.23–7.40	[66,85]
b	m	$2.95{\cdot}10^{-10}$ - $5.53{\cdot}10^{-10}$	[55]
$\dot{\bar{\varepsilon}}^p$	s^{-1}	10^4 - 10^7 (*)	[4–6, 47, 86]
K_c (T = 25–595 °C)	–	40	[68]
Ω (T = 25 °C)	–	38	[68]
Ω (T = 595 °C)	–	40	[68]
c_γ (T = 25 °C)	–	0	[68]
c_γ (T = 595 °C)	–	0.4	[68]
k	JK^{-1}	$1.38{\cdot}10^{-23}$	–
ρ_{eq}	m^{-2}	10^{10} - 10^{13}	[52,66,68]
D_α	m^2s^{-1}	$5{\cdot}10^{-6}$	[72]
D_β	m^2s^{-1}	$3{\cdot}10^{-7}$	[72]
$T_{\beta\text{-transus}}$	K	1163	–
D_{p0}	m^2s^{-1}	10^{-8} - 10^{-4}	[63,87,88]
Q_p	J	$1.61{\cdot}10^{-19}$ - $1.2{\cdot}10^{-18}$	[89,90]
$n_a{}^p$	–	2	[68]
$N_a{}^l$	m^{-2}	10^{19}	[68]
ΔS_{vf}	JK^{-1}	$6.9{\cdot}10^{-24}$ - $2.76{\cdot}10^{-23}$	[66,91]
Q_{vf}	J	$1.9{\cdot}10^{-19}$	[92]
χ	–	0.1	[66]
α (T = 25 °C)	–	2.3	[68]
α (T = 595 °C)	–	1.7	[68]
Ω_0	m^3	$1.76{\cdot}10^{-29}$	[93]
D_{vm}	m^2s^{-1}	13.7	[66]

(*) following the methodology described in [79], the strain rate follows a linear dependence from $1.71{\cdot}10^4$, at z = 0, to $1.67{\cdot}10^4$, at z = 400 μm.

dislocations can be modelled by Eqs. (10)-(14) with the values shown in Table 4. A dislocation density value of $8{\cdot}10^{11}$-$2.4{\cdot}10^{12}$ cm^{-2} in the surface is generated by LSP. During the post-LSP annealing a restoration process takes place. Applying the model with Eqs. (14)-(24) and values of Table 4, using the starting value $c_v = 0$ [78], the working temperature studied in this paper (595 °C), and considering time $t \to \infty$, it is found that the dislocation density over time reaches a stable limit value that is approximately $2–3{\cdot}10^{11}$ cm^{-2} in the surface, well above that of untreated samples. Thus, a certain level of the dislocations produced by the LSP treatment will remain even at high temperature. In Fig. 8, the curve that models the dislocation density generated by LSP and the ones that models the remaining dislocation density at the annealing temperature using the parameters of Table 4 is also shown.

In this model, the variable that depends on the depth, z, and that allows obtaining a dislocation density profile is the strain rate, $\dot{\bar{\varepsilon}}^p(z)$. This dependence has been obtained following the methodology described in [79].

A small overestimation of the dislocation density by the model is observed since the model considers an average Burger vector of all dislocations whose motion can take place. This means that low Burger vector dislocations motion takes place, most probably, basal dislocations, what is coherent with [68,78]. Despite this, the observed experimental data fit the model reasonably and can perfectly be considered as representative of the effects induced in the material by the LSP treatment. The level of dislocation densities is coherent with the reported limits of dislocation densities for high strain-hardened metals ($\sim 10^{12}$ cm^{-2}) [80–83]. The physical reason for the remanence of a certain level of dislocation density is that high density dislocations entangle each other and prevent the movement of other dislocations [84]. High-speed dislocations accommodate the very high strain rate deformation during LSP, and planar dislocations and networks of dislocation cells and sub grains are produced [47]. This makes even more difficult for dislocations to entangle and move freely to reduce its density.

The reduction in grain size in the first few micrometres below the surface due to a considerable increase in dislocation density produced by the LSP treatment is consistent with the observed increase in hardness. High-speed dislocations accommodate the very high strain rate deformation during LSP, and networks of dislocation cells and sub grains are produced. Increased dislocation density and reduced grain size lead to increased hardness. These effects produced by LSP are partially reduced by the post-LSP annealing that simulates the working conditions in which the alloy is usually used. However, a certain reduction in grain size and an appreciable increase in dislocation density and hardness with respect to the material in the state prior to LSP treatment remain. This shows that the LSP treatment improves in Ti-6Al-4 V the resistance to the severe thermal conditions in which this alloy is employed.

3.5. Residual stresses

The root cause for the described modifications of mechanical properties is the LSP induced deep and saturated compressive residual stresses, or stress fields, in subsurface layers. As indicated in a previous section, the LSP laser pulses create a plasma of metallic material that, when expanding, generates a shock wave into the material. The wave in turn produces a plastic deformation that embeds mechanical stresses.

There are theoretical models and numerical analysis that relate LSP to residual stresses [5,14]. There are also measurements on Ti-6Al-4 V [5,14,16,47], each with its own particular LSP features. They all report values of maximum compressive LSP induced stresses of 600–700 MPa, within the 65–75% of the materials yield strength.

In this study, residual stress fields have been measured by two techniques: the hole-drilling method and X-ray diffraction. Additionally, some estimations are provided by means of the experimental strains obtained by neutron diffraction considering the pseudo-strain corrections. As presented above, two main issues may limit the applicability of the neutron diffraction measurements to obtain residual stresses in this particular case. First, diffraction measurements were only possible in a different crystallographic plane for each measurement direction. Secondly, measurements could not be obtained in the ND of the samples. The results of the measurements according to the different methods are presented below. The maximum and minimum stress in-depth profiles in the RD-TD plane (see Fig. 2), σ_{max} and σ_{min}, are presented. These profiles are also compared with RD and TD stresses, σ_{RD} and σ_{TD}, respectively, achieved by X-ray diffraction. To obtain the whole stress tensor in a measurement point with neutron diffraction, six measurements are required. In this study, only the RD and TD were measured, assuming that the maximum and minimum stress are very similar to the ones of the RD and TD. In the hole-drilling and X-ray diffraction measurements, it is observed that σ_{max} and σ_{min} are practically the same as σ_{RD} and σ_{TD}, corroborating the assumption made in neutron diffraction. For simplicity, only σ_{max} and σ_{min} are shown in the hole-drilling and X-ray diffraction results. All samples exhibit about 1 mm deep compressively stressed surface layer. Fig. 9 shows the residual stresses measured in the samples treated with LSP by the three methods.

Table 5 shows the main values of the results obtained by the hole-drilling measurement. High level compressive residual stresses are clearly present in the laser peened samples (LB/TB). The general trend of the in-depth compressive residual stress is characterized. Minor compressive stresses at materials surface and a sudden increase of the maximum compressive stress until 0.23 mm, where the peak compression is achieved (≅ −600 MPa). After the application of the annealing treatment, this stress profiles are clearly softened but not completely reduced, a certain level of residual stresses still remaining. At 595ºC/1 h, a significant compressive residual stress relaxation (about 65–70%) occurs. The minimum compressive stress direction is almost coincident with the RD and the maximum in-plane stress with the TD in all the treatment conditions.

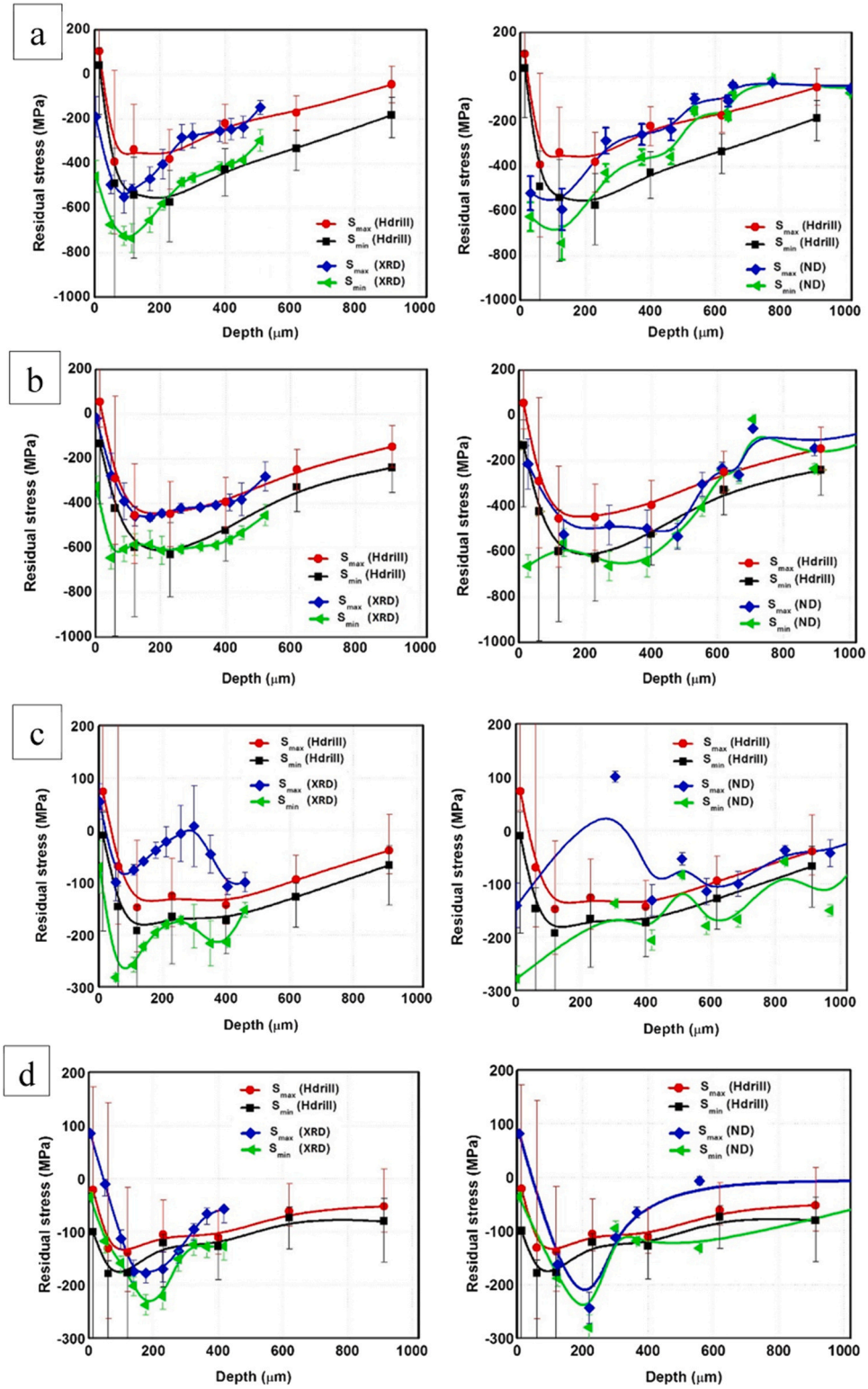

Fig. 9. (a)-(b) Maximum and minimum residual stresses for LSP treated samples LB-TB, respectively, obtained by hole-drilling, neutron, and X-ray diffraction methods. Fig. 9. (c)-(d) Maximum and minimum residual stresses for LSP treated and post aged samples LC-TC, respectively, obtained by hole-drilling, neutron, and X-ray diffraction methods.

Table 6 shows the results analogous to those obtained in the hole-drilling test but for the X-ray diffraction experiments. In all samples except for TC, stresses in RD, σ_{RD}, are more compressive than stresses in TD, σ_{TD}, and are similar to $\sigma_{min.}$ In the same way, σ_{TD} is similar to $\sigma_{max.}$ In the TC sample a somehow different behavior occurs. In this case, σ_{RD} and σ_{TD} have almost the same values. σ_{TD} is slightly more compressive than σ_{RD}, but the difference is neglectable.

As it was also seen in the hole-drilling results, after the application of the annealing treatment, a significant compressive residual stress relaxation (about 60–70%) occurs, but, again, it can be clearly observed that stresses are not fully eliminated. They remain to a certain level. In TC, the maximum σ_{max} value is achieved at the surface and corresponds to a tensile stress. The $|\sigma_{max}|_{max}$ value indicated refers to the most compressive stress.

Table 5
Approximate main values of the results obtained by the hole-drilling measurement.

Hole-Drilling Residual Stresses	σ_{max} (13 µm) (MPa)	σ_{min} (13 µm) (MPa)	$\|\sigma_{max}\|_{max}$ (MPa)	$\|\sigma_{min}\|_{max}$ (MPa)	Depth $\|\sigma_{max}\|_{max}$ (µm)	Depth $\|\sigma_{min}\|_{max}$ (µm)
LB	105	41	379	573	230	230
TB	55	-132	453	629	120	230
LC	96	19	143	182	120	120
TC	-16	-95	133	177	120	60

Table 7 shows the results obtained in the neutron diffraction experiment. As it happened in X-ray diffraction, σ_{RD} are more compressive than σ_{TD} in all samples, except in the TC sample, where σ_{TD} are more compressive than σ_{RD}.

As a reference condition value, the measurement at 1.216 mm has been chosen as d_0. Good agreement is achieved with Hole-drilling measurements. This suggests the appropriateness of the developed simplified method, but further research is required.

As a main result, and as it was also seen in the other two test results, after the application of the annealing treatment, a significant compressive residual stress relaxation (about 55–75%) occurs, but a certain level of stresses is finally remaining.

On the surface of the material, hole-drilling measurements, and the results of the X-ray diffraction technique show, as expected, several differences. The hole-drilling technique is capable of measuring residual stresses up to 1 mm in depth, while the X-ray diffraction technique is limited to the measurement of deformations in very shallow layers (10–15 µm) although it can reach up to approximately 0.5 mm using electro-polishing. However, it is well known that the hole-drilling technique has high sources of error and inaccuracy near the surface and is very sensitive to experimental errors and the choice of data entered in the software [27]. This causes the values to present higher errors than those presented by the X-ray diffraction technique.

Because of the high levels of material deformation and the applied high deformation rates, the application of LSP treatments is typically running with the induction of large in-depth strain gradients near the surface [5,6,94]. This implies large uncertainties in the hole-drilling results, so that this method can be sometimes unable to capture the subtlety of large stress gradients. Therefore, X-ray can be taken into greater consideration in the first microns in depth. There is no inconsistency between both methods considering that X-ray diffraction results are inside the uncertainty window provided by the hole-drilling method. Although it has been possible to take measurements at greater depths with electro-polishing, greater reliability would be expected from the hole-drilling results from a certain depth, since uncertainties are reduced in the hole-drilling technique. Although electro-polishing is known for not being aggressive in the introduction of additional stress states, it is a source of additional uncertainty. That is why the X-ray diffraction results most immediate to the surface could be taken as representative to build globally a reliable curve of compressive residual stresses together with the hole-drilling results from a certain depth.

There is evidence [95] showing that the TD in rolled samples has an upper elastic limit (20% approximately) in comparison with the RD. It would be reasonable, then, to think that the peening direction is not enough to compensate the anisotropy. In this study, experimental results suggest that the minimum residual stresses correspond approximately to the RD, which would be consistent with the fact that the RD has a lower elastic limit and reaches higher plastic deformations. X-ray diffraction results show a slight enhancement of the minimum stress, σ_{min}, for LB condition with respect to TB condition. This is as expected considering that the peening direction usually sets the minimum principal stress in isotropic materials.

In the case of the samples that have been submitted to subsequent heat treatment, it seems that the small subtle differences between conditions originated by different peening directions are diminished, and, in both cases, LC and TC, similar results are achieved. In the LC sample, stresses are more intense in the RD, while in the TC sample stresses are more intense in the TD. In both cases, peak stresses are maintained around − 200 MPa after the heat treatment. This suggests that parts made of this alloy that are LSP-treated would improve their working life under high temperature conditions in comparison with parts that do not have an LSP treatment. The tendency to form tensile stresses in the surface is justified by the thermal effect due to the transfer of heat between the plasma and the surface of the material [8,96].

Regarding neutron diffraction measurements, due to the crystallographic texture of the samples, it was not possible to obtain measurements in the ND and different crystallographic planes were measured in the RD and TD. Nevertheless, it is well known that LSP is characterised for predominantly inducing in-plane residual stresses, so the assumption of plane stress in the RD-TD plane is adequate [16, 97–99]. In addition, the Kröner model described above used to calculate the residual stresses provides uncertainty intervals that are not very wide. This indicates that neutron diffraction measurements have a very acceptable level of precision and that they can be taken as representative of the whole material. These measurements confirm the results obtained by the hole-drilling and X-ray diffraction. LB residual stresses are more compressive than TB residual stresses and, in both samples, stresses in the RD are more compressive than in the TD. Similarly, the most compressive stresses are not achieved at the surface, but a little bit below. In TB, although the peak compressive stress is less intense than in LB, it is found at a greater depth than in LB. In this case, the fact of a more intense tension at a shallower depth competes with a slightly less intense tension at a slightly greater depth.

Comparing the residual stresses profiles measured by X-ray diffraction and neutron diffraction near the surface, it is observed that those corresponding to XRD are more tensile than the ones obtained by neutron diffraction and, a few micrometres below, they become more compressive than the neutron diffraction ones. In X-ray diffraction, the gage volume (GV) generated by the incident and diffracted beams is very small (GV rhombus diagonal lower than 50 µm) compared to the one generated in neutron diffraction. In this case, the width of the incident and diffracted neutron beams is 0.6 mm, but the rhombus diagonal of the GV, that indicates the length of the set of diffracting grains that contribute to the

Table 6
Approximate main values of the results obtained in the X-ray diffraction experiment.

X-ray Diffraction Residual Stresses	σ_{max} surface (MPa)	σ_{min} surface (MPa)	$\|\sigma_{max}\|_{max}$ (MPa)	$\|\sigma_{min}\|_{max}$ (MPa)	Depth $\|\sigma_{max}\|_{max}$ (µm)	Depth $\|\sigma_{min}\|_{max}$ (µm)
LB	-190	-460	550	735	89.5	114
TB	-20	-325	460	645	167.5	48
LC	55	-70	100	280	53.5	53.5
TC	85	-35	180	240	175	175

Table 7
Approximate main values of the results obtained in the neutron diffraction experiment.

Neutron Diffraction Residual Stresses	σ_{max} closest to the surface (MPa)	σ_{min} closest to the surface (MPa)	$\|\sigma_{max}\|_{max}$ (MPa)	$\|\sigma_{min}\|_{max}$ (MPa)	Depth $\|\sigma_{max}\|_{max}$ (μm)	Depth $\|\sigma_{min}\|_{max}$ (μm)
LB	-520 (31 μm)	-625 (31 μm)	595	745	128	128
TB	-215 (27 μm)	-665 (27 μm)	535	665	480	27
LC	-140 (2 μm)	-280 (2 μm)	140	280	138	138
TC	80 (6 μm)	-37 (6 μm)	245	280	220	220

measurement, is much higher (~1.6 mm), because the 2θ is very low (~45º). This implies that the residual stress gradient measured is smoothed with respect to the actual one, that is better caught at the surface by the X-ray method.

Summing up the experimental Residual Stress profiles obtained by the three determination methods, it is clearly found that, first, they are highly coherent and, second, they all show clearly that the induction of intense compressive residual stresses fields in the samples is effectively reached by the designed LSP treatments, with a minor influence due to the possible original manufacturing anisotropy shown by the samples.

However, a major result of the analysis specifically sought concerns the ability of the LSP treatments to confer to the treated material a thermally stable degree of compressive state protecting it under severe thermal working conditions. In particular, it has been clearly obtained, that a major effect of the high strain rates (of the order of 10^6 s^{-1} and higher) applied to the material positively induce microstructural transformations responsible for the remanence of compression residual stress fields even after the application of thermal aging cycles that normally involve a total relaxation of residual stresses of thermal origin.

Several authors have also reported this effect for other metal alloys [100,101] and, in view of the obtained results, a deeper investigation of the microstructure and dislocation density by means of specific differential methods (namely, i.e., TEM microscopy) is required to finally assess the actual buildup mechanisms and stability of these dislocations. However, the final consequence can be obtained that, by application of the LSP technique to the considered material, its properties range with respect to thermal cycles design can be effectively enlarged.

4. Conclusions

In the present study, the analysis of the thermal stability of residual stresses induced in Ti-6Al-4 V by high density LSP treatments has been undertaken. The LSP-induced effects include modifications in roughness, microstructure, microhardness, dislocation density and residual stresses as the main macroscopic effect responsible for the mechanical behavior of the treated components. In order to check such thermal stability, which is considered as critical from the point of view of in-service performance of these components, LSP-treated samples have been subjected to heat treatments representative of the most exigent in-service conditions. The maintenance of the originally induced residual stresses fields has been specifically analyzed by means of the combination of different complementary residual stress measurement methods aiming at an optimum sensitivity of the corresponding residual stress profiles by considering the region at which each method offers the highest accuracy.

The main observed effects along the pursued study are:

1. As a main microstructural effect, the LSP treatment produces a large increase in dislocation density, an effect that is slightly reduced after post-LSP annealing, but that has been clearly observed to remain after this kind of aging cycle to an extent higher than three orders of magnitude.
2. In a consistent way, the LSP treatment produces a considerable grain size reduction in the first in-depth ~20–40 μm (80% in the immediate surface) as a result of the dislocation networks and sub cells generated by the referred increase in the dislocation density. Correspondingly, the LSP treatment is able to increase the surface hardness of the treated samples significantly over the relaxed state obtained by annealing prior to LSP treatments and, although after post LSP thermal aging treatments, the surface hardness is observed to moderately relax, a significant hardened state is still maintained. The residual stresses obtained by means of the three complementary measurement techniques (neutron diffraction, X-ray diffraction and hole drilling) are fully consistent with the numerical models previously published by the authors and the measured modifications in microstructure, microhardness and residual stresses fields can be appropriately traced to the increase in dislocation density created by the LSP treatment.
3. All these coherent results have been confirmed by a suitable combination of theoretical evaluations and experimental material characterization techniques providing a considerable degree of reliability positively assessing the improved mechanical performance of the Ti-6Al-4 V alloy against heavy duty thermal conditions.
4. Although additional investigations relating some of them (especially the elucidation of the concrete mechanisms of generation of non-reversible dislocations at the high deformation rates typically induced by LSP), all these results jointly support the consequence that, by application of the LSP technique to the considered material, its properties range with respect to thermal cycles design can be effectively enlarged.

CRediT authorship contribution statement

W. Warzanskyj: Data curation, Formal analysis, Investigation, Methodology, Software, Visualization, Writing – original draft. **I. Angulo**: Data curation, Formal analysis, Investigation, Software, Visualization, Writing – review & editing. **F. Cordovilla**: Investigation, Methodology, Writing – review & editing. **M. Díaz**: Investigation, Methodology, Writing – review & editing. **J.A. Porro**: Investigation, Writing – review & editing. **A. García-Beltrán**: Writing – review & editing. **S. Cabeza**: Data curation, Formal analysis, Investigation, Methodology, Writing – review & editing. **J.L. Ocaña**: Conceptualization, Funding acquisition, Project administration, Resources, Supervision, Validation, Writing – review & editing.

Data Availability

The authors do not have permission to share data.

Declaration of Competing Interest

The authors declare that they have no known competing financial interests or personal relationships that could have appeared to influence the work reported in this paper.

Acknowledgements

The reported XRD residual stress measurements were performed at the IMDEA Materials Institute (Madrid, Spain). The authors are indebted for excellent technical assistance. Work partly developed under support of the Institut Laue-Langevin campaign ILL-4/2019–1-02–274 and the granted internship of WWP. The authors are indebted to Dr. Th. Pirling for his fundamental scientific support. Work partly supported by MINECO (Spain; Grants MAT2012–37782, MAT2015–63974-C4–2-R and PID2019–104351GB-C21).

References

[1] U. Sanchez-Santana, C. Rubio-González, G. Gomez-Rosas, J.L. Ocaña, C. Molpeceres, J.A. Porro, M. Morales, Wear and friction of 6061-T6 aluminum alloy treated by laser shock processing, Wear 260 (7–8) (2006) 847–854, https://doi.org/10.1016/j.wear.2005.04.014

[2] Y. Sano, N. Mukai, K. Okazaki, M. Obata, Residual stress improvement in metal surface by underwater laser irradiation, Nucl. Instrum. Methods Phys. Res. Sect. B: Beam Interact. Mater. At. 121 (1–4) (1997) 432–436, https://doi.org/10.1016/S0168-583X(96)00551-4

[3] P. Peyre, R. Fabbro, P. Merrien, H.P. Lieurade, Laser shock processing of aluminium alloys. Application to high cycle fatigue behaviour, Mater. Sci. Eng.: A 210 (1–2) (1996) 102–113, https://doi.org/10.1016/0921-5093(95)10084-9

[4] C. Correa, L.R. De Lara, M. Díaz, J.A. Porro, A. García-Beltrán, J.L. Ocaña, Influence of pulse sequence and edge material effect on fatigue life of Al2024-T351 specimens treated by laser shock processing, Int. J. Fatigue 70 (2015) 196–204, https://doi.org/10.1016/j.ijfatigue.2014.09.015

[5] C. Correa, A. Gil-Santos, J.A. Porro, M. Díaz, J.L. Ocaña, Eigenstrain simulation of residual stresses induced by laser shock processing in a Ti6Al4V hip replacement, Mater. Des. 79 (2015) 106–114, https://doi.org/10.1016/j.matdes.2015.04.048

[6] C. Correa, D. Peral, J.A. Porro, M. Díaz, L.R. De Lara, A. García-Beltrán, J.L. Ocaña, Random-type scanning patterns in laser shock peening without absorbing coating in 2024-T351 Al alloy: a solution to reduce residual stress anisotropy, Opt. Laser Technol. 73 (2015) 179–187, https://doi.org/10.1016/j.optlastec.2015.04.027

[7] M. Morales, J.L. Ocaña, C. Molpeceres, J.A. Porro, A. García-Beltrán, Model based optimization criteria for the generation of deep compressive residual stress fields in high elastic limit metallic alloys by ns-laser shock processing, Surf. Coat. Technol. 202 (11) (2008) 2257–2262, https://doi.org/10.1016/j.surfcoat.2007.12.007

[8] P. Peyre, C. Carboni, P. Forget, G. Beranger, C. Lemaitre, D. Stuart, Influence of thermal and mechanical surface modifications induced by laser shock processing on the initiation of corrosion pits in 316L stainless steel, J. Mater. Sci. 42 (16) (2007) 6866–6877, https://doi.org/10.1007/s10853-007-1502-4

[9] J.A. Porro, C. Molpeceres, M. Morales, J.L. Ocaña, Generación de un campo de tensiones residuales de compresión en aluminio 2024-T351 mediante tratamiento por onda de choque generada por láser (Laser Shock Processing), Óptica Pura Y. Apl. 40 (1) (2007) 73–78 ISSN 0030-3917.

[10] C.S. Montross, T. Wei, L. Ye, G. Clark, Y.W. Mai, Laser shock processing and its effects on microstructure and properties of metal alloys: a review, Int. J. Fatigue 24 (10) (2002) 1021–1036, https://doi.org/10.1016/S0142-1123(02)00022-1

[11] C. Rubio-González, C. Felix-Martinez, G. Gomez-Rosas, J.L. Ocaña, M. Morales, J.A. Porro, Effect of laser shock processing on fatigue crack growth of duplex stainless steel, Mater. Sci. Eng.: A 528 (3) (2011) 914–919, https://doi.org/10.1016/j.msea.2010.10.020

[12] P.J. Golden, A. Hutson, V. Sundaram, J.H. Arps, Effect of surface treatments on fretting fatigue of Ti–6Al–4V, Int. J. Fatigue 29 (7) (2007) 1302–1310, https://doi.org/10.1016/j.ijfatigue.2006.10.005

[13] I. Altenberger, R.K. Nalla, Y. Sano, L. Wagner, R.O. Ritchie, On the effect of deep-rolling and laser-peening on the stress-controlled low-and high-cycle fatigue behavior of Ti–6Al–4V at elevated temperatures up to 550C, Int. J. Fatigue 44 (2012) 292–302, https://doi.org/10.1016/j.ijfatigue.2012.03.008

[14] Z. Zhou, S. Bhamare, G. Ramakrishnan, S.R. Mannava, K. Langer, Y. Wen, V.K. Vasudevan, Thermal relaxation of residual stress in laser shock peened Ti–6Al–4V alloy, Surf. Coat. Technol. 206 (22) (2012) 4619–4627, https://doi.org/10.1016/j.surfcoat.2012.05.022

[15] Designation, A.S.T.M. E837: Standard Test Method for Determining Residual Stresses by the Hole-Drilling Strain-Gage Method. Annual Book of ASTM Standards, *3*(1). https://doi.org/10.1520/E0837–13A.

[16] J.L. Ocaña, J.L. González-Carrasco, M. Lieblich, S. Barriuso, J.A. Porro, L. Ruiz de Lara, J.A. Santiago, Compressive residual stresses and associated surface modifications induced in Ti6Al4V by laser shock processing, Materials Science Forum Vol. 879 Trans Tech Publications Ltd.,, 2017, pp. 1408–1413, https://doi.org/10.4028/www.scientific.net/MSF.879.1408

[17] J.L. Ocaña, M. Morales, J.A. Porro, M. Blasco, C. Molpeceres, D. Iordachescu, C. Rubio-González, Induction of engineered residual stresses fields and associate surface properties modification by short pulse laser shock processing, Materials Science Forum Vol. 638 Trans Tech Publications Ltd.,, 2010, pp. 2446–2451, https://doi.org/10.4028/www.scientific.net/MSF.638-642.2446

[18] J.L. Ocaña, M. Morales, J.A. Porro, D. Iordachescu, M. Díaz, L.R. De Lara, C. Correa, Mechanical properties enhancement of high reliability metallic materials by laser shock processing, Materials Science Forum Vol. 706 Trans Tech Publications Ltd.,, 2012, pp. 2565–2570, https://doi.org/10.4028/www.scientific.net/MSF.706-709.2565

[19] J.L. Ocaña, C. Molpeceres, J.A. Porro, G. Gómez, M. Morales, Experimental assessment of the influence of irradiation parameters on surface deformation and residual stresses in laser shock processed metallic alloys, Appl. Surf. Sci. 238 (1–4) (2004) 501–505, https://doi.org/10.1016/j.apsusc.2004.05.246

[20] W. Rae, S. Rahimi, Effect of stress relaxation on the evolution of residual stress during heat treatment of Ti-6Al-4V, MATEC Web of Conferences Vol. 321 EDP Sciences,, 2020, p. 11001, https://doi.org/10.1051/matecconf/202032111001

[21] ISO, U. (1999). 4287: 1999, Especificación geométrica de productos (GPS). *Calidad superficial: Método del perfil. Términos, definiciones y parámetros del estado superficial. (ISO 4287: 1997+ Technical Corrigendum 1)*.

[22] American Society for Testing and Materials (ASTM), Standard Guide for Preparation of Metallographic Specimens, ASTM E3-11, American Society for Testing and Materials, United States of America, 2017⟨https://doi.org/10.1520/E0003-11R17⟩.

[23] M. Trtica, B. Gakovic, D. Batani, T. Desai, P. Panjan, B. Radak, Surface modifications of a titanium implant by a picosecond Nd: YAG laser operating at 1064 and 532 nm, Appl. Surf. Sci. 253 (5) (2006) 2551–2556, https://doi.org/10.1016/j.apsusc.2006.05.024

[24] A. Muiruri, M. Maringa, W. du Preez, Evaluation of dislocation densities in various microstructures of additively manufactured Ti6Al4V (ELI) by the method of x-ray diffraction, Materials 13 (23) (2020) 5355, https://doi.org/10.3390/ma13235355

[25] B.D. Cullity, J.W. Weymouth, Elements of X-Ray diffraction, Am. J. Phys. 25 (6) (1957) 394–395, https://doi.org/10.1119/1.1934486

[26] U. Trdan, J.A. Porro, J.L. Ocaña, J. Grum, Laser shock peening without absorbent coating (LSPwC) effect on 3D surface topography and mechanical properties of 6082-T651 Al alloy, Surf. Coat. Technol. 208 (2012) 109–116, https://doi.org/10.1016/j.surfcoat.2012.08.048

[27] Peral Jiménez, D. (2017). *Desarrollo de métodos para la acotación de la incertidumbre en medidas de tensiones residuales en materiales metálicos tratados por LSP* (Doctoral dissertation, Industriales).

[28] G.S. Schajer, M. Steinzig, Full-field calculation of hole drilling residual stresses from electronic speckle pattern interferometry data, Exp. Mech. 45 (6) (2005) 526–532, https://doi.org/10.1177/0014485105059553

[29] Fitzpatrick, M.E., Fry, A.T., Holdway, P., Kandil, F.A., Shackleton, J., & Suominen, L. (2005). Determination of residual stresses by X-ray diffraction.

[30] P.S. Prevey, X-Ray Diffraction Residual Stress Techniques 10 ASM International, ASM Handbook, 1986, pp. 380–392.

[31] Ezeilo, A.N., & Webster, G.A. Advances in Neutron Diffraction for Engineering Residual Stress Measurements. *Textures and Microstructures*, *33*(1–4), 151–171.

[32] G. Bruno, B.D. Dunn, The precise measurement of Ti6Al4V microscopic elastic constants by means of neutron diffraction, Meas. Sci. Technol. 8 (11) (1997) 1244, https://doi.org/10.1088/0957-0233/8/11/006

[33] W.F. Gale, T.C. Totemeier (Eds.), Smithells metals reference book, Elsevier, 2003ISBN 9780750675093.

[34] T. Pirling, G. Bruno, P.J. Withers, SALSA—A new instrument for strain imaging in engineering materials and components, Mater. Sci. Eng.: A 437 (1) (2006) 139–144, https://doi.org/10.1016/j.msea.2006.04.083

[35] T. Pirling, Precise analysis of near surface neutron strain imaging measurements, Procedia Eng. 10 (2011) 2147–2152, https://doi.org/10.1016/j.proeng.2011.04.355

[36] A.D. Evans, A. King, T. Pirling, P. Peyre, P.J. Withers, Characterisation of residual stresses generated by laser shock peening by neutron and synchrotron diffraction, Engineering Against Fracture, Springer,, Dordrecht, 2009, pp. 383–398, https://doi.org/10.1007/978-1-4020-9402-6_31

[37] J.R. Kornmeier, M. Hofmann, V. Luzin, J. Gibmeier, J. Saroun, Fast neutron surface strain scanning with high spatial resolution, Mater. Charact. 154 (2019) 53–60, https://doi.org/10.1016/j.matchar.2019.05.031

[38] A.M. Stapleton, S.L. Raghunathan, I. Bantounas, H.J. Stone, T.C. Lindley, D. Dye, Evolution of lattice strain in Ti–6Al–4V during tensile loading at room temperature, Acta Mater. 56 (20) (2008) 6186–6196, https://doi.org/10.1016/j.actamat.2008.08.030

[39] L. Crespo, M. Hierro-Oliva, S. Barriuso, V. Vadillo-Rodríguez, M.Á. Montealegre, L. Saldaña, N. Vilaboa, On the interactions of human bone cells with Ti6Al4V thermally oxidized by means of laser shock processing, Biomed. Mater. 11 (1) (2016) 015009, https://doi.org/10.1088/1748-6041/11/1/015009

[40] R.K. Nalla, I. Altenberger, U. Noster, G.Y. Liu, B. Scholtes, R.O. Ritchie, On the influence of mechanical surface treatments—deep rolling and laser shock peening—on the fatigue behavior of Ti–6Al–4V at ambient and elevated temperatures, Mater. Sci. Eng.: A 355 (1–2) (2003) 216–230, https://doi.org/10.1016/S0921-5093(03)00069-8

[41] S. Spanrad, J. Tong, Characterisation of foreign object damage (FOD) and early fatigue crack growth in laser shock peened Ti–6Al–4V aerofoil specimens, Mater. Sci. Eng.: A 528 (4–5) (2011) 2128–2136, https://doi.org/10.1016/j.proeng.2010.03.188

[42] S. Srinivasan, D.B. Garcia, M.C. Gean, H. Murthy, T.N. Farris, Fretting fatigue of laser shock peened Ti–6Al–4V, Tribology Int. 42 (9) (2009) 1324–1329, https://doi.org/10.1016/j.triboint.2009.04.014

[43] A.S.T.M. Standard, Standard Test Methods for Determining Average Grain Size, ASTM Standard, 2013, pp. E112–*10*, https://doi.org/10.1520/E0112-13

[44] J.L. Ocaña, J.A. Porro, M. Díaz, L. Ruiz de Lara, A. García-Beltrán, J.A. Santiago, D. Peral, Improvement of surface and mechanical properties of high strength

metallic alloys by laser shock processing, Adv. Mater. Process. Technol. 3 (1) (2017) 12–22, https://doi.org/10.1080/2374068X.2016.1247241
[45] W. Guo, R. Sun, B. Song, Y. Zhu, F. Li, Z. Che, P. Peng, Laser shock peening of laser additive manufactured Ti6Al4V titanium alloy, Surf. Coat. Technol. 349 (2018) 503–510, https://doi.org/10.1016/j.surfcoat.2018.06.020
[46] G. Ranjith Kumar, G. Rajyalakshmi, S. Swaroop, S. Arul Xavier Stango, U. Vijayalakshmi, Laser shock peening wavelength conditions for enhancing corrosion behaviour of titanium alloy in chloride environment, J. Braz. Soc. Mech. Sci. Eng. 41 (3) (2019) 1–18, https://doi.org/10.1007/s40430-019-1633-y
[47] S.J. Lainé, K.M. Knowles, P.J. Doorbar, R.D. Cutts, D. Rugg, Microstructural characterisation of metallic shot peened and laser shock peened Ti–6Al–4V, Acta Mater. 123 (2017) 350–361, https://doi.org/10.1016/j.actamat.2016.10.044
[48] P.R. Smith, M.J. Shepard, P.S. Prevey, A.H. Clauer, Effect of power density and pulse repetition on laser shock peening of Ti-6Al-4V, J. Mater. Eng. Perform. 9 (1) (2000) 33–37, https://doi.org/10.1361/105994900770346259
[49] Y. Shadangi, K. Chattopadhyay, S.B. Rai, V. Singh, Effect of LASER shock peening on microstructure, mechanical properties and corrosion behavior of interstitial free steel, Surf. Coat. Technol. 280 (2015) 216–224, https://doi.org/10.1016/j.surfcoat.2015.09.014
[50] X.D. Ren, W.F. Zhou, Y.P. Ren, S.D. Xu, F.F. Liu, S.Q. Yuan, J.J. Huang, Dislocation evolution and properties enhancement of GH2036 by laser shock processing: Dislocation dynamics simulation and experiment, Mater. Sci. Eng.: A 654 (2016) 184–192, https://doi.org/10.1016/j.msea.2015.12.007
[51] S. Nagarjuna, K. Balasubramanian, D.S. Sarma, Effect of prior cold work on mechanical properties and structure of an age-hardened Cu–1.5 wt% Ti alloy, J. Mater. Sci. 32 (13) (1997) 3375–3385, https://doi.org/10.1023/A:1018608430443
[52] R.W.K. Honeycombe, The Plastic Deformation of Metals, Edward Arnold Pub, 1984 ISBN 0-7131-3468-2.
[53] J.Z. Lu, L.J. Wu, G.F. Sun, K.Y. Luo, Y.K. Zhang, J. Cai, X.M. Luo, Microstructural response and grain refinement mechanism of commercially pure titanium subjected to multiple laser shock peening impacts, Acta Mater. 127 (2017) 252–266, https://doi.org/10.1016/j.actamat.2017.01.050
[54] R.K. Gupta, V.A. Kumar, C. Mathew, G.S. Rao, Strain hardening of titanium alloy Ti6Al4V sheets with prior heat treatment and cold working, Mater. Sci. Eng.: A 662 (2016) 537–550, https://doi.org/10.1016/j.msea.2016.03.094
[55] D. Hull, S.B. Brody, Introduction to Dislocations, Am. J. Phys. 36 (2) (1968) 174-174, https://doi.org/10.1119/1.1974472
[56] T. Simm, The Use of Diffraction Peak Profile Analysis in Studying the Plastic Deformation of Metals, The University of Manchester, United Kingdom, 2013.
[57] Y. Bergitrom, The plastic deformation of metals–a dislocation model and its applicability, Rev. Powder Metall. Phys. Ceram. 2 (2) (1983) 79–265.
[58] R.V.V. Nicho, Symposium on internal stresses in metals and alloys, Nature (1949) *164*.
[59] H. Mecking, U.F. Kocks, Kinetics of flow and strain-hardening, Acta Metall. 29 (11) (1981) 1865–1875, https://doi.org/10.1016/0001-6160(81)90112-7
[60] Fisk, M. (2011). *Modelling of induction heat treatment in a manufacturing chain* (Doctoral dissertation, Luleå tekniska universitet).
[61] D.L. Holt, Dislocation cell formation in metals, J. Appl. Phys. 41 (8) (1970) 3197–3201, https://doi.org/10.1063/1.1659399
[62] W. Roberts, Y. Bergström, The stress-strain behaviour of single crystals and polycrystals of face-centered cubic metals—a new dislocation treatment, Acta Metall. 21 (4) (1973) 457–469, https://doi.org/10.1016/0001-6160(73)90203-4
[63] M. Zamani, H. Dini, A. Svoboda, L.E. Lindgren, S. Seifeddine, N.E. Andersson, A.E. Jarfors, A dislocation density based constitutive model for as-cast Al-Si alloys: effect of temperature and microstructure, Int. J. Mech. Sci. 121 (2017) 164–170, https://doi.org/10.1016/j.ijmecsci.2017.01.003
[64] G.A. Sargent, A.P. Zane, P.N. Fagin, A.K. Ghosh, S.L. Semiatin, Low-temperature coarsening and plastic flow behavior of an alpha/beta titanium billet material with an ultrafine microstructure, Metall. Mater. Trans. A 39 (12) (2008) 2949–2964, https://doi.org/10.1007/s11661-008-9650-y
[65] Domkin, K. (2005). *Constitutive models based on dislocation density: Formulation and implementation into finite element codes* (Doctoral dissertation, Luleå tekniska universitet).
[66] L.E. Lindgren, K. Domkin, S. Hansson, Dislocations, vacancies and solute diffusion in physical based plasticity model for AISI 316L, Mech. Mater. 40 (11) (2008) 907–919, https://doi.org/10.1016/j.mechmat.2008.05.005
[67] M. Militzer, W.P. Sun, J.J. Jonas, Modelling the effect of deformation-induced vacancies on segregation and precipitation, Acta Metall. Et. Mater. 42 (1) (1994) 133–141, https://doi.org/10.1016/0956-7151(94)90056-6
[68] B. Babu, L.E. Lindgren, Dislocation density based model for plastic deformation and globularization of Ti-6Al-4V, Int. J. Plast. 50 (2013) 94–108, https://doi.org/10.1016/j.ijplas.2013.04.003
[69] Babu, B. (2018). *Mechanism-based flow stress model for Ti-6Al-4V: applicable for simulation of additive manufacturing and machining* (Doctoral dissertation, Luleå University of Technology).
[70] D.A. Porter, K.E. Easterling, Phase Transformations in Metals and Alloys (Revised Reprint), CRC Press, 2009, https://doi.org/10.1201/9781439883570
[71] J. Friedel, Dislocations, Pergamon Press, New York, 1964.
[72] Y. Mishin, C. Herzig, Diffusion in the Ti–Al system, Acta Mater. 48 (3) (2000) 589–623, https://doi.org/10.1016/S1359-6454(99)00400-0
[73] F. Prinz, A.S. Argon, W.C. Moffatt, Recovery of dislocation structures in plastically deformed copper and nickel single crystals, Acta Metall. 30 (4) (1982) 821–830, https://doi.org/10.1016/0001-6160(82)90080-3
[74] C.H. Johnson, S.K. Richter, C.H. Hamilton, J.J. Hoyt, Static grain growth in a microduplex Ti–6Al–4V alloy, Acta Mater. 47 (1) (1998) 23–29, https://doi.org/10.1016/S1359-6454(98)00341-3
[75] R.E. Reed-Hill, R. Abbaschian, R. Abbaschian, Physical metallurgy principles Vol. 17 Van Nostrand,, New York, 1973.
[76] P. Shewmon (Ed.), Diffusion in solids, Springer, 2016ISBN 0-87339-105-5.
[77] Chan, R.W., & Haasen, P. (1996). Physical Metallurgy, 4th revised and enhanced ed. ISBN 9780080538945.
[78] J.M. Rodríguez, S. Larsson, J.M. Carbonell, P. Jonsén, Dislocation density based flow stress model applied to the PFEM simulation of orthogonal cutting processes of Ti-6Al-4V, Materials 13 (8) (2020) 1979, https://doi.org/10.3390/ma13081979
[79] I. Angulo, F. Cordovilla, A. García-Beltrán, N.S. Smyth, K. Langer, M.E. Fitzpatrick, J.L. Ocaña, The effect of material cyclic deformation properties on residual stress generation by laser shock processing, Int. J. Mech. Sci. 156 (2019) 370–381, https://doi.org/10.1016/j.ijmecsci.2019.03.029
[80] M.A. Meyers, Mechanical Behavior of Materials, Aircr. Eng. Aerosp. Technol. (2009), https://doi.org/10.1108/aeat.2009.12781bae.001
[81] R.W. Hertzberg, H. Saunders, Deform. Fract. Mech. Eng. Mater. (1985), https://doi.org/10.1115/1.3264456
[82] W.D. Callister Jr, D.G. Rethwisch, Fundamentals of materials science and engineering: an integrated approach, John Wiley & Sons,, 2020 ISBN 978-1-119-24925-2.
[83] J.P. Hirth, J. Lothe, T. Mura, Theory of dislocations, J. Appl. Mech. 50 (2) (1983) 476, https://doi.org/10.1115/1.3167075
[84] X. Nie, W. He, S. Zang, X. Wang, J. Zhao, Effect study and application to improve high cycle fatigue resistance of TC11 titanium alloy by laser shock peening with multiple impacts, Surf. Coat. Technol. 253 (2014) 68–75, https://doi.org/10.1016/j.surfcoat.2014.05.015
[85] T.R. Bieler, S.L. Semiatin, The origins of heterogeneous deformation during primary hot working of Ti–6Al–4V, Int. J. Plast. 18 (9) (2002) 1165–1189, https://doi.org/10.1016/S0749-6419(01)00057-2
[86] Y. Yang, H. Zhang, H. Qiao, Microstructure characteristics and formation mechanism of TC17 titanium alloy induced by laser shock processing, J. Alloy. Compd. 722 (2017) 509–516, https://doi.org/10.1016/j.jallcom.2017.06.127
[87] A. Arieli, A. Rosen, Superplastic deformation of Ti-6Al-4V alloy, Metall. Trans. A 8 (10) (1977) 1591–1596, https://doi.org/10.1007/BF02644864
[88] M. Ferrante, E.V. Pigoretti, Diffusion bonding of TI-6AL-4V to AISI 316L stainless steel: mechanical resistance and interface microstructure, J. Mater. Sci. 37 (13) (2002) 2825–2833, https://doi.org/10.1023/A:1015845822629
[89] W.A. Bryant, Correlation of data on the hot deformation of Ti-6Al-4V, J. Mater. Sci. 10 (10) (1975) 1793–1797, https://doi.org/10.1007/BF00554942
[90] Frost, H.J., Ashby, M.F., & Maps, D.M. (1982). the Plasticity and Creep of Metals and Ceramics. *Deformation-Mechanism Maps*.
[91] D.H. Ruiz, L.M. Gribaudo, A.M. Monti, Self-diffusion in the hexagonal structure of Zirconium and Hafnium: computer simulation studies, Mater. Res. 8 (4) (2005) 431–434, https://doi.org/10.1590/S1516-14392005000400012
[92] I.I. Novikov, V.V. Roshchupkin, N.A. Semashko, L.K. Fordeeva, Experimental investigation of vacancy effects in pure metals, J. Eng. Phys. 39 (6) (1980) 1316–1319, https://doi.org/10.1007/BF00825700
[93] S. Akram, S.H.I. Jaffery, M. Khan, M. Fahad, A. Mubashar, L. Ali, Numerical and experimental investigation of Johnson–Cook material models for aluminum (Al 6061-T6) alloy using orthogonal machining approach, Adv. Mech. Eng. 10 (9) (2018), https://doi.org/10.1177/1687814018797794
[94] U. Trdan, M. Skarba, J.A. Porro, J.L. Ocaña, J. Grum, Application of massive laser shock processing for improvement of mechanical and tribological properties, Surf. Coat. Technol. 342 (2018) 1–11, https://doi.org/10.1016/j.surfcoat.2018.02.084
[95] M. Morales, C. Correa, J.A. Porro, C. Molpeceres, J.L. Ocaña, Thermomechanical modelling of stress fields in metallic targets subject to laser shock processing, Int. J. Struct. Integr. (2011), https://doi.org/10.1108/17579861111108617
[96] S. Zabeen, K. Langer, M.E. Fitzpatrick, Effect of texture on the residual stress response from laser peening of an aluminium-lithium alloy, J. Mater. Process. Technol. 251 (2018) 317–329, https://doi.org/10.1016/j.jmatprotec.2017.07.032
[97] Y. Hu, R.V. Grandhi, Efficient numerical prediction of residual stress and deformation for large-scale laser shock processing using the eigenstrain methodology, Surf. Coat. Technol. 206 (15) (2012) 3374–3385, https://doi.org/10.1016/j.surfcoat.2012.01.050
[98] A.S. Gill, Z. Zhou, U. Lienert, J. Almer, D.F. Lahrman, S.R. Mannava, V.K. Vasudevan, High spatial resolution, high energy synchrotron x-ray diffraction characterization of residual strains and stresses in laser shock peened Inconel 718SPF alloy, J. Appl. Phys. 111 (8) (2012) 084904, https://doi.org/10.1063/1.3702890
[99] C. Wang, K. Li, X. Hu, H. Yang, Y. Zhou, Numerical study on laser shock peening of TC4 titanium alloy based on the plate and blade model, Opt. Laser Technol. 142 (2021) 107163, https://doi.org/10.1016/j.optlastec.2021.107163
[100] K.Y. Luo, J.Z. Lu, Y.K. Zhang, J.Z. Zhou, L.F. Zhang, F.Z. Dai, C.Y. Cui, Effects of laser shock processing on mechanical properties and micro-structure of ANSI 304 austenitic stainless steel, Mater. Sci. Eng.: A 528 (13–14) (2011) 4783–4788, https://doi.org/10.1016/j.msea.2011.03.041
[101] A.Y. Chen, H.H. Ruan, J. Wang, H.L. Chan, Q. Wang, Q. Li, J. Lu, The influence of strain rate on the microstructure transition of 304 stainless steel, Acta Mater. 59 (9) (2011) 3697–3709, https://doi.org/10.1016/j.actamat.2011.03.005